The Astrophysical Journal, 649:788–806, 2006 October 1

THE NATURE OF INTERSTELLAR GAS TOWARD THE PLEIADES REVEALED IN ABSORPTION LINES

A. M. Ritchey,[1] M. Martinez,[1,2] K. Pan,[3,4] S. R. Federman,[1,5] and D. L. Lambert[6]

Received 2006 February 17; accepted 2006 June 7

ABSTRACT

We present high-resolution, high signal-to-noise ratio absorption-line observations of CN, Ca II, Ca I, CH^+, and CH along 20 lines of sight toward members of the Pleiades. The acquired data enable the most detailed study to date of the interaction between cluster stars and the surrounding interstellar gas. Total equivalent widths are consistent with previous investigations, except where weaker features are detected owing to our greater sensitivity. Mean *b*-values for the molecular species indicate that toward most of the Pleiades, CH is associated with the production of CH^+ rather than CN. An analysis of radial velocities reveals a kinematic distinction between ionized atomic gas and molecular and neutral gas. Molecular components are found with velocities in the local standard of rest of either $\sim$+7 or $\sim$+9.5 km s^{-1}, with the higher velocity components being associated with the strongest absorption. Atomic gas traced by Ca II shows a strong central component at $v_{\rm LSR} \sim +7$ km s^{-1}, exhibiting velocity gradients indicative of cloud-cluster interactions. Gas density estimates derived from measured CH/CH^+ column density ratios show good agreement with those inferred from H_2 rotational populations, yielding typical values of $n \sim 50$ cm^{-3}. Our models do not include the important time-dependent effects on CH^+ formation, which may ultimately be needed to extract physical conditions in these clouds.

Subject headings: ISM: abundances — ISM: kinematics and dynamics — ISM: molecules — open clusters and associations: individual (Pleiades)

1. INTRODUCTION

The interstellar medium (ISM) in the vicinity of the Pleiades is a rich environment for the study of processes that result from the interactions between stellar photons and the gas and dust clouds of interstellar space. The stars of this cluster were not formed out of the surrounding material visible as reflection nebulosity. Rather, the spatial association of the stars and the interstellar gas is the result of a chance encounter between the cluster and one or more approaching clouds (White 2003). Such collisions precipitate numerous radiative processes, including the photoionization of atomic and molecular species, the photodissociation of molecules such as CH and H_2, and the photoelectric heating of diffuse gas by dust grains stimulated by ultraviolet radiation, all of which may help to explain some peculiarities of the ISM near the Pleiades.

Two such peculiarities are the great strength of CH^+ absorption lines observed toward many cluster members (White 1984a) and the large amount of H_2 in rotationally excited states (Spitzer et al. 1974). While these anomalies may be related, a rigorous chemical model of CH^+ production in the Pleiades, and elsewhere in the ISM, remains to be developed. CH^+ is unable to form at the low temperature of diffuse clouds because the reaction leading to its formation, $C^+ + H_2 \rightarrow CH^+ + H$, is endothermic with an activation energy of $\Delta E/k = 4640$ K. Elitzur & Watson (1978, 1980) showed that the above reaction can produce sufficient amounts of CH^+ if the gas is heated by an interstellar shock. However, subsequent observations failed to detect a corresponding overabundance of OH molecules resulting from a similar endothermic reaction (Federman et al. 1996b). Several groups (Draine & Katz 1986; Pineau des Forêts et al. 1986) employed magnetohydrodynamic (MHD) shocks to lessen the problem with the overproduction of OH, but even their models yielded OH column densities in excess of observations. The velocity shifts between CH and CH^+ absorption lines predicted by these shock models have also not been detected (e.g., Gredel et al. 1993). Alternate theories for a nonthermal origin of CH^+ have since been proposed. Federman et al. (1996a) considered the motions of C^+ ions influenced by the passage of Alfvén waves against a static background of cold neutral gas. Their model predicts CH^+, CH, and OH column densities in line with observations, but requires an additional mechanism to account for observed HCO^+ abundances. More recently, nonequilibrium chemistry was investigated by Joulain et al. (1998) and Falgarone et al. (2005). These authors ascribed the transient heating of localized regions of the cold diffuse medium to intermittent bursts of turbulent dissipation by either MHD shocks or coherent small-scale vortices. Such models may be appropriate for many Galactic sight lines, yet the observational evidence in the Pleiades favors heating either by H_2 dissociation or by dust photoelectron emission, rather than shocks, as the agent responsible for CH^+ formation (White 1984b).

Precise measurements of CN, CH^+, and CH column densities in the Pleiades interstellar gas can offer new insight into the chemical reaction networks active in these diffuse clouds. At the same time, highly sensitive observations of Ca II and, to a lesser extent, Ca I can be used to trace the kinematic effects of the interaction occurring between interstellar gas and the stellar radiation field in great detail and on large spatial scales. The earlier investigation by White (1984a), comprising spectra for 15 Pleiades members, analyzed interstellar absorption from the above atomic and molecular species, but the moderate velocity resolutions ($\sim$3–8 km s^{-1}) allowed detections of only one component per sight line. Later studies capable of detecting many line-of-sight components, such as the ultra–high-resolution survey by Crane et al. (1995)

[1] Department of Physics and Astronomy, University of Toledo, Toledo, OH 43606; aritchey@physics.utoledo.edu, steven.federman@utoledo.edu.
[2] Department of Aeronautical and Astronautical Engineering, University of Washington, Seattle, WA 98195; marleen@u.washington.edu.
[3] Department of Physics and Astronomy, Bowling Green State University, Bowling Green, OH 43403.
[4] Apache Point Observatory, New Mexico State University, P.O. Box 59, Sunspot, NM 88349; kpan@apo.nmsu.edu.
[5] Guest Observer, McDonald Observatory, University of Texas, Austin, TX 78712.
[6] W. J. McDonald Observatory, University of Texas, Austin, TX 78712; dll@astro.as.utexas.edu.

TABLE 1
STELLAR AND OBSERVATIONAL DATA

HD	Name	Type	$E(B-V)$ (mag)	B (mag)	α (J2000.0)	δ (J2000.0)	d (pc)	τ_{exp} (s)
23288.....	16 Tau	B7 IV	0.10	5.41	03 44 48.22	+24 17 22.1	103 ± 11	3 × 1200
23302.....	17 Tau	B6 III	0.05	3.61	03 44 52.54	+24 06 48.0	114 ± 12	2 × 600
23324.....	18 Tau	B8 V	0.05	5.58	03 45 09.74	+24 50 21.3	113 ± 11	2 × 1800
23338.....	19 Tau	B6 IV	0.04	4.20	03 45 12.49	+24 28 02.2	114 ± 14	3 × 600
23408.....	20 Tau	B7 III	0.07	3.81	03 45 49.61	+24 22 03.9	110 ± 13	2 × 600
23410.....		A0 V	0.08	6.92	03 45 48.82	+23 08 49.7	103 ± 11	4 × 1800
23432.....	21 Tau	B8 V	0.07	5.73	03 45 54.48	+24 33 16.2	119 ± 13	2 × 1800
23441.....	22 Tau	B9 V	0.06	6.42	03 46 02.90	+24 31 40.4	109 ± 11	2 × 1800
23480.....	23 Tau	B6 IV	0.10	4.11	03 46 19.57	+23 56 54.1	110 ± 13	3 × 600
23512.....		A1 V	0.35	8.47	03 46 34.20	+23 37 26.5	...	8 × 1800
23568.....		B9.5 V	0.07[a]	6.85	03 46 59.40	+24 31 12.4	150 ± 23	4 × 1800
23629.....	24 Tau	A2 V	−0.03	6.30	03 47 21.04	+24 06 58.6	...	3 × 1800
23630.....	η Tau	B7 III	0.04	2.81	03 47 29.08	+24 06 18.5	113 ± 13	2 × 300
23753.....		B8 V	0.04	5.38	03 48 20.82	+23 25 16.5	104 ± 10	2 × 1200
23850.....	27 Tau	B8 III	0.04	3.54	03 49 09.74	+24 03 12.3	117 ± 14	2 × 600
23862.....	28 Tau	B8 Vp	0.03	4.97	03 49 11.22	+24 08 12.2	119 ± 12	3 × 900
23873.....		B9.5 V	0.02[a]	6.59	03 49 21.75	+24 22 51.4	125 ± 14	3 × 1800
23923.....		B8 V	0.06[a]	6.12	03 49 43.53	+23 42 42.7	117 ± 13	2 × 1800
23964.....		B9.5 Vp	0.11	6.80	03 49 58.06	+23 50 55.3	159 ± 39	4 × 1800
24076.....		A2 V	0.03[a]	7.02	03 50 52.43	+23 57 41.3	102 ± 10	4 × 1800

NOTE.—Units of right ascension are hours, minutes, and seconds, and units of declination are degrees, arcminutes, and arcseconds.
[a] Reddening values for these stars were updated in White (2003).

of interstellar CH^+ and CH and the high-resolution survey by Welty et al. (1996) of Ca II K, included only a few of the brightest Pleiades members in their sample. Most recently, high-resolution observations were made by White et al. (2001) of 36 Pleiades stars, both members and nonmembers, in the Na I D lines and of 12 of these stars in the Na I ultraviolet doublet. The full analysis of these data (White 2003) revealed considerable complexity and star-to-star variation in the atomic gas traced by neutral sodium, leading to an extensive spatial schematic of cloud-cluster interactions in which two clouds were presumed to be interacting with the UV radiation field of the Pleiades and also with each other. One of the primary motivations for the present investigation was to obtain equally high-quality data for the other important optical tracers of the ISM toward a large number of targets in the Pleiades so that a complete picture of the interaction between interstellar gas clouds and the stars of the cluster may be constructed.

In this paper, high-resolution, high signal-to-noise ratio observations of CN, Ca II, Ca I, CH^+, and CH toward 20 Pleiades members allow us to study cloud-cluster interactions and the implications for the chemistry of the local ISM with a precision unmatched by previous investigations. We describe our observations and detail the process of data reduction in § 2. In § 3 we present the results of Gaussian fitting the observed profiles and compare our measurements to those from the literature. The analysis of our observations appears in § 4, with particular attention paid to the spatial distribution of atomic and molecular velocity components (§ 4.1). We examine Na I/Ca II column density ratios in § 4.2 and derive physical conditions in § 4.3. In § 5 we interpret our findings in light of the conceptual schematic of cloud-cluster interactions offered by White (2003) and summarize our principal results in § 6.

2. OBSERVATIONS AND DATA REDUCTION

We observed 20 stars in the Pleiades using the high-resolution mode (cs21) of the 2dcoudé spectrograph (Tull et al. 1995) on the Harlan J. Smith 2.7 m telescope at McDonald Observatory in 2002 January. The choice of sight lines came from the list in White et al. (2001), from which only those stars with secure membership in the Pleiades cluster were included in our survey. Stellar and observational data for the stars in our sample appear in Table 1. Specifically, the HD number, name, spectral type, reddening, B magnitude, equatorial coordinates (J2000.0), distance, and total exposure time on each star are presented. The spectral types and $E(B-V)$ values come from White et al. (2001), while the B magnitudes and equatorial coordinates were obtained from the SIMBAD database, operated at the Centre de Données Astronomiques de Strasbourg (CDS), France. It is most appropriate to list B magnitudes because our instrumental setup had a central wavelength near 4000 Å. The parallax for each star was obtained from *Hipparcos* measurements (Perryman 1997), when available, and used to calculate the distance given in Table 1. Additional information on the program stars is available from Table 2 of White et al. (2001). For reference, Figure 1 shows the distribution of observed sight lines in the Pleiades centered on η Tau.

The cross-dispersed echelle spectrometer of the 2dcoudé spectrograph was configured in a manner identical to that described by Pan et al. (2004) for their McDonald Observatory spectra. When combined with a 2048 × 2048 CCD, this configuration made possible the search for interstellar absorption from many species with a single exposure. In particular, the spectral coverage allowed for the detection of absorption features from CN near 3874 Å, Ca II K at 3933 Å, Ca I λ4226, CH^+ λ4232, and CH λ4300. Each star was observed at least twice, with a maximum exposure time of 30 minutes per frame to minimize the effect of cosmic rays. Calibration exposures for dark current were obtained on the first night of the run, while exposures for bias correction and flat fielding were taken each night, and Th-Ar comparison spectra were obtained every 2–3 hr. By measuring the width of thorium emission lines in the comparison spectra, the resolution for these observations is determined to be about 1.7 km s^{-1}, equivalent to a resolving power of $R \sim 175{,}000$.

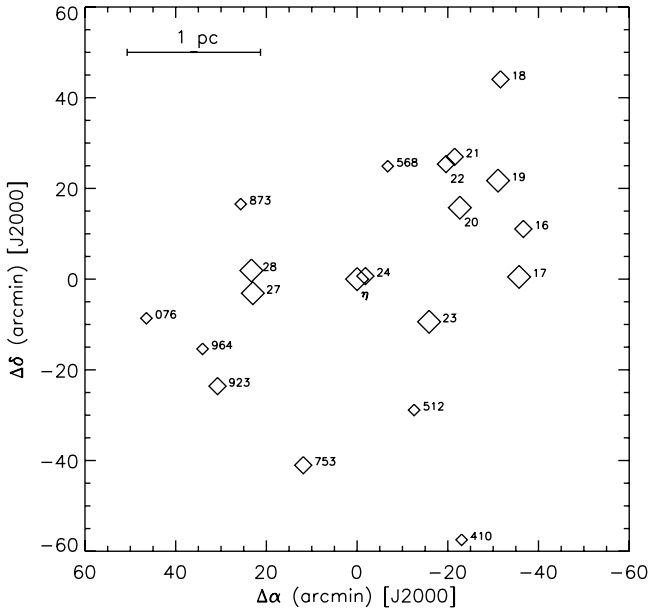

FIG. 1.—Distribution of observed Pleiades stars in relative equatorial coordinates centered on η Tau [α(J2000.0) = $03^h47^m29\overset{s}{.}08$, δ(J2000.0) = $+24°06'18\overset{''}{.}5$]. The label next to each symbol is either the last three digits of the HD number or the Flamsteed or Bayer designation. Decreasing symbol size denotes three magnitude ranges: $B < 5.0$, $5.0 < B < 6.5$, and $6.5 < B$. This key is used in Figs. 6, 7, and 8.

Standard Image Reduction and Analysis Facility (IRAF) routines were used for bias correction, cosmic-ray removal, and flat fielding of the raw image data. One-dimensional spectra were extracted from the processed images and were calibrated in wavelength using the Th-Ar comparison spectra and then Doppler corrected. In regions where interstellar absorption lines were expected, individual spectra were cut from each stellar exposure with sufficient continua on both sides, typically 2 Å. All spectra for the same species toward the same star were summed to yield a higher signal-to-noise ratio (S/N) in the final spectrum. The S/Ns obtained in this way yielded 3 σ upper limits of about 2 mÅ on CN absorption and about 1 mÅ above 4000 Å. Further details concerning the many steps in the data reduction process can be found by consulting Pan et al. (2004), with the caveat that no smoothing or additional processing was performed on the data presented here. Stellar spectra were normalized to unity by fitting Legendre polynomials, of the lowest possible order, to regions free of interstellar absorption. This process proceeded without complication, except in the case of HD 23964. The spectra for all of our targeted species toward this star showed strong stellar features near the position of the expected interstellar lines. For Ca II K, we were able to normalize the stellar feature because of the strength of the interstellar lines and their location away from the core of the stellar profile. But for CN, Ca I, CH^+, and CH, the stellar features could not be removed by normalization.

Figures 2–4 present the final normalized spectra for Ca II K, CH^+, and CH, respectively. The panels are arranged to approximate the spatial relationship among sight lines so that a comparison might be made of absorption profiles in different regions of the cluster (see Fig. 2). Figure 5 presents the final normalized spectrum for CN absorption toward HD 23512, the only sight line in our sample with a detectable amount of this molecule. Because

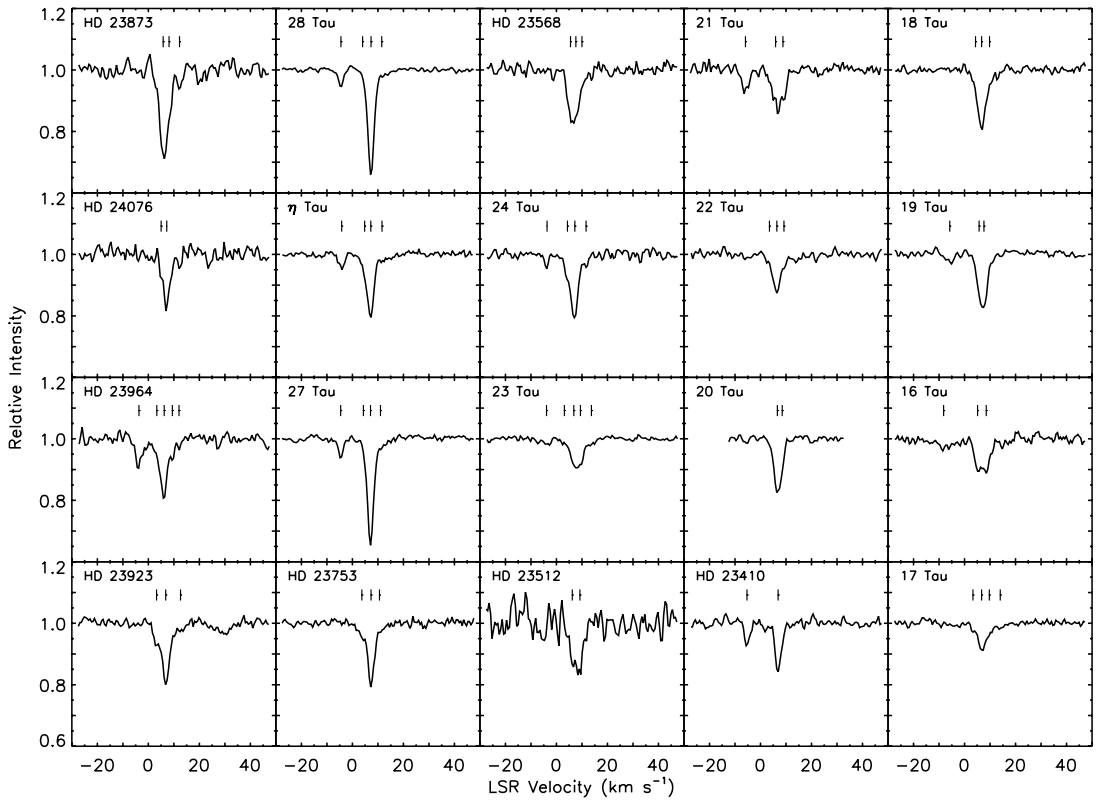

FIG. 2.—Observed Ca II spectra arranged to approximate the spatial relationships among sight lines. Spectra toward the left (right) of the figure correspond to sight lines in the eastern (western) part of the cluster. Likewise, spectra toward the top (bottom) of the figure correspond to sight lines in the north (south). See Fig. 1 for the actual distribution of sight lines. The vertical tick marks indicate velocity components.

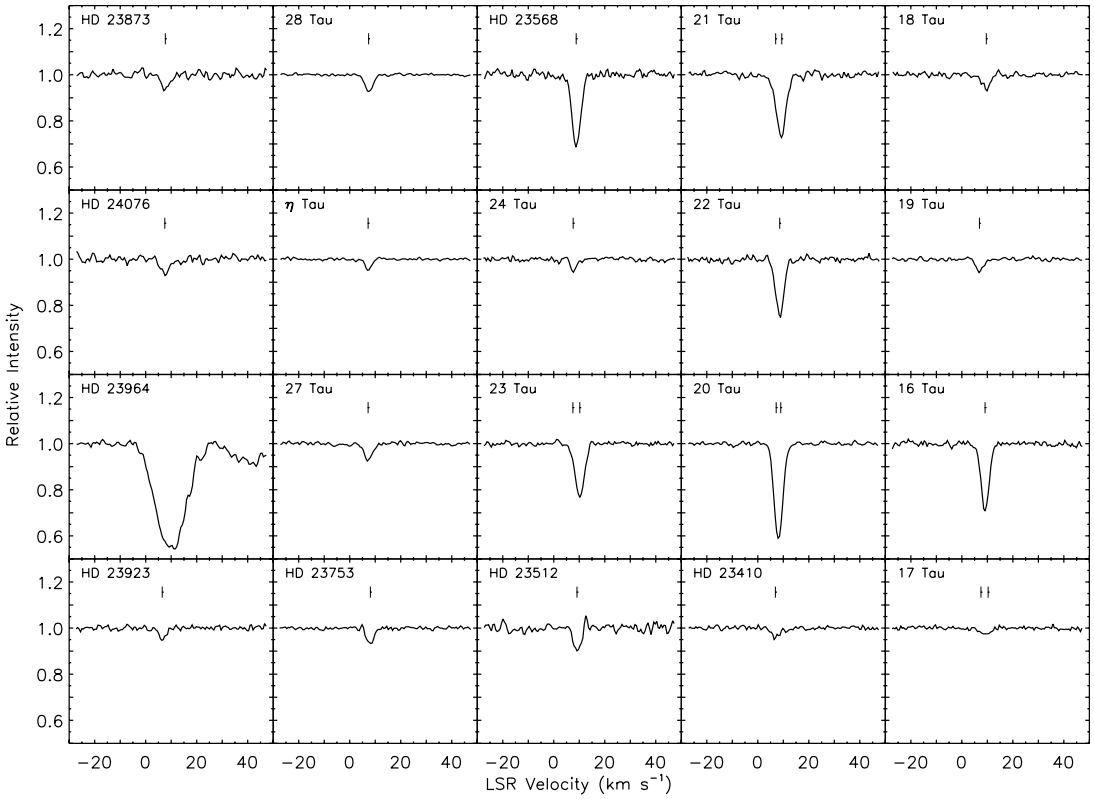

FIG. 3.—Observed CH^+ spectra arranged as in Fig. 2. Strong stellar features in the spectrum of HD 23964 prevented us from discerning any interstellar lines here and in Fig. 4.

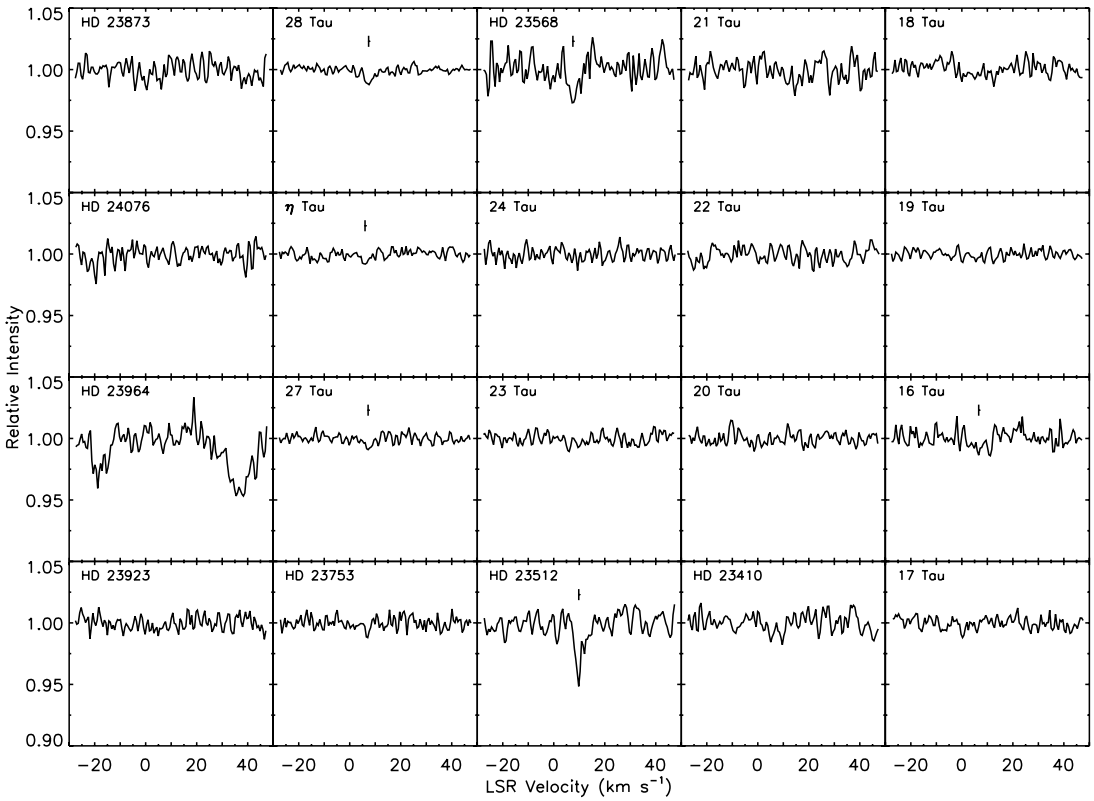

FIG. 4.—Observed CH spectra arranged as in Fig. 2. For HD 23512, the intensity scale has been reduced by a factor of 2.

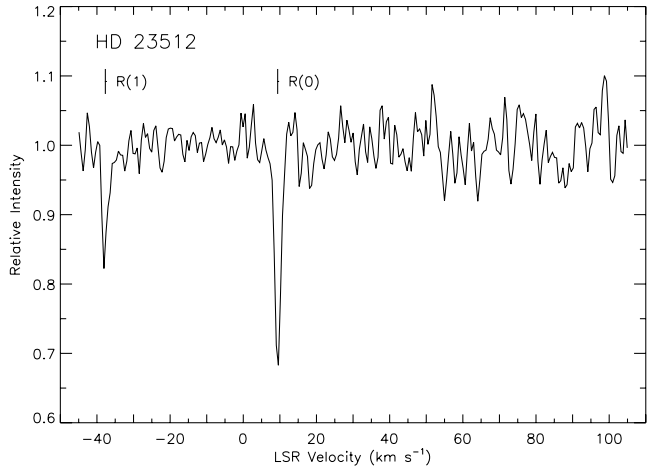

FIG. 5.—Observed CN spectrum toward HD 23512. The zero point in velocity corresponds to the central wavelength of the $R(0)$ line. The zero points of the $R(1)$ and $P(1)$ lines would occur at $v_{\rm LSR} = -47.2$ and $+89.0$ km s^{-1} on this scale, respectively. The figure shows positive detections of both the $R(0)$ and $R(1)$ lines. The $P(1)$ line is below the detection limit.

no Ca I absorption (stronger than $\sim$1 mÅ) is detected along any of the observed sight lines, the spectra for this species are not given. These negative results are not unexpected considering the survey of Ca I by Welty et al. (2003), which found predominantly quite weak Ca I lines.

3. OBSERVATIONAL RESULTS

The resolution and S/N of our observations were high enough to allow the detection of multiple components of Ca II K and CH^+ and to permit the first positive detections of CN and CH toward a few of the observed stars. The lines were relatively weak, enabling us to fit simple Gaussians to the components, yielding values for the equivalent width (W_λ), radial velocity in the local standard of rest ($v_{\rm LSR}$), and full width at half-maximum (FWHM) for each component. The Doppler parameter (b-value) was obtained from the measured line width (FWHM), corrected for the instrumental width determined from thorium emission lines in the Th-Ar spectra. Uncertainties in W_λ were derived from the rms variations in the normalized continuum and the width of the line for a specific component. They do not include errors in the placement of the continuum, but this is assumed to have a negligible effect. When no component was detected, 3 σ upper limits were calculated by adopting a typical width for the species in question. Subsequent profile synthesis including Λ-doubling for the CH features yielded no significant change in fitted W_λ. Thus, the analysis of this paper rests solely on the results of our Gaussian fits.

The moderately complex component structures of the Ca II K and CH^+ absorption profiles were constrained by the derived b-values. In general, no component narrower than 0.4 km s^{-1} or broader than 2.5 km s^{-1} was accepted, where the upper limit to b is 1.5 times the mean value for Ca II found by Pan et al. (2005). We note that this restriction plays at most a minor role in the component analysis. In some cases, it was necessary to compare the velocity of a CH^+ component to that of Ca II K to determine its legitimacy. As discussed in some detail in Pan et al. (2004), because Ca II is the most widely distributed of the observed species, if any other species has a component at a particular $v_{\rm LSR}$, then Ca II should also have a component at that velocity. Based on our resolution, an agreement within 1.5 km s^{-1} was deemed adequate. The final component structure for a given line of sight resulted from using the fewest number of components, subject to the above criteria, which adequately fit the observed profile and left the residuals indistinguishable from the noise in the continuum. Naturally, this approach presumes that the velocity structure along a line of sight is constant across species. To test this assumption, we computed the difference between the velocities found for associated CH^+ and Ca II components, $v(CH^+) - v$(Ca II). The average difference in velocity for components detected in both species is +0.3 km s^{-1}. To the extent that this result is comparable to the estimated uncertainty ($\sigma_v \sim 0.2$–0.3 km s^{-1}), we can be reasonably assured that our fits reveal the true component structure for a given line of sight.

As seen in Figure 2, interstellar absorption from Ca II K is detected along all 20 sight lines, resulting in 65 individual components. We note that our study detects 50% more absorption components in Ca II than White et al. (2001) found in their Na I observations for the same directions. Figure 3 shows that CH^+ absorption is just as pervasive, yet only 23 components are identified. No detection of CH^+ toward HD 23964 is possible because the core of the stellar line discussed in § 2 directly coincides with the expected position of the interstellar feature. Marginal detections of CH toward five of the observed stars are indicated in Figure 4. A stronger component is detected toward HD 23512, a sight line that passes through a known molecular cloud (Federman & Willson 1984). The spectrum of CN toward this star (Fig. 5) clearly shows the absorption features of the $R(0)$ and $R(1)$ transitions of this molecule, but the weaker $P(1)$ line is below the detection limit.

3.1. *Total Equivalent Widths*

An extensive comparison of our values of total W_λ with those found in the literature appears in Table 2 for the five species studied. A thorough examination reveals that our values, obtained by summing all of the individual components along a line of sight, are consistent with most previous determinations, many of which derive from only one resolved component. Of the 37 spectra in our investigation with counterparts in the literature, significant discrepancies in total W_λ (greater than 3 σ) are noted in only six. Stellar contamination most likely affected the measurements by White (1984a) of Ca II toward 20 Tau and 22 Tau and of CH toward HD 23512. White's (1973) measurement of Ca II toward η Tau is also suspected of suffering from inadequate normalization of a stellar feature. Our value for W_λ(Ca II) toward 27 Tau is substantially larger than the consistent values given by three previous investigations (Younan & Dufton 1984; White 1984a; Marschall & Hobbs 1972). This is due to our ability to detect weaker features in the wings of the more prominent absorption line. Similarly, the determination of $W_\lambda(CH^+)$ toward HD 23753 by Frisch (1972) was affected by her detection limit of $\sim$6 mÅ. In the case of nondetections, since our upper limits are significantly lower than those of all preceding studies, our results further constrain the detectable amount of absorption from these less abundant species along the observed sight lines. We also point out that while Federman (1982) claimed a detection of CH toward 20 Tau, it is but a 2.5 σ detection and is consistent with our quoted upper limit. The average uncertainties in our measurements of W_λ for individual components fall below 1 mÅ for all four detected species: specifically, $\sigma_W = 0.7$ mÅ for CN, 0.4 mÅ for Ca II, and 0.3 mÅ for CH^+ and CH. Since the uncertainties from the literature are usually greater than 1 mÅ, our measurements are among the most precise now available.

3.2. *Column Densities*

Column densities for individual components were interpolated from curves of growth based on the measured equivalent

TABLE 2

Comparison of Total Equivalent Widths

Reference	W_λ(Ca II) (mÅ)	W_λ(Ca I) (mÅ)	W_λ(CH^+) (mÅ)	W_λ(CH) (mÅ)	W_λ(CN) (mÅ)
			16 Tau		
1	10.7 ± 0.7	≤0.9	16.0 ± 0.4	0.5 ± 0.3	≤1.8
2	10.8 ± 1.4	≤2.4	19.5 ± 1.1	≤4.4	≤5.5
3	15 ± 3	...	20 ± 2	≤13	...
4	...	...	18.5	...	...
			17 Tau		
1	6.5 ± 0.5	≤0.7	1.9 ± 0.3	≤0.6	≤1.4
2	6.0 ± 1.5	≤3.5	≤2.4	≤2.0	≤3.6
5	4.4 ± 0.4	...	...	...	...
6	4	...	...	...	...
			18 Tau		
1	11.5 ± 0.5	≤0.8	3.0 ± 0.3	≤0.8	≤1.2
2	≤13	≤4.0	≤4.6	≤4.0	≤7.7
			19 Tau		
1	11.6 ± 0.5	≤0.6	2.8 ± 0.2	≤0.5	≤1.2
2	12.3 ± 1.5	≤4.5	4.0 ± 1.3	≤4.1	≤3.7
3	≤13	...	≤13	≤13	...
6	9	...	...	...	...
			20 Tau		
1	9.0 ± 0.4	≤0.8	24.4 ± 0.3	≤0.7	≤1.5
2	12.4 ± 1.1	≤2.2	22.2 ± 0.5	≤1.9	≤2.1
4	...	...	20.4	...	...
6	8	...	...	...	...
7	...	...	24.2	≤0.2	...
8	...	...	23.3 ± 0.3	...	...
9	...	...	20.2 ± 1.8	1.3 ± 0.5	...
10	...	...	23.5	...	...
11	...	...	31.0	...	...
12	...	...	25.4	...	...
			21 Tau		
1	12.4 ± 0.9	≤1.2	18.2 ± 0.7	≤1.1	≤2.4
2	13.4 ± 1.8	≤6.9	20.0 ± 1.5	≤7.9	≤5.7
3	15 ± 2	...	25 ± 3	≤13	...
			22 Tau		
1	7.3 ± 0.6	≤1.0	14.0 ± 0.4	≤0.9	≤1.6
2	17.7 ± 3.2	≤8.1	≤8.7	≤6.7	≤10
			23 Tau		
1	9.0 ± 0.4	≤0.6	15.0 ± 0.4	≤0.6	≤1.3
2	10.3 ± 1.1	≤2.9	14.1 ± 0.5	≤2.6	≤3.5
3	≤13	...	25 ± 5	≤13	...
4	...	...	14.2	...	...
6	7	...	...	...	...
7	...	...	16.2	≤3.1	...
8	...	...	14.0 ± 0.2	...	...
9	...	...	12.5 ± 2.2	≤2.9	...
11	...	...	16.0	...	...
			HD 23512		
1	11.2 ± 1.7	≤2.2	5.1 ± 0.6	4.3 ± 0.6	8.7 ± 0.7
2	≤22	≤13	≤14	23 ± 5	≤29
13	...	...	...	5.3 ± 0.8	≤10.0

TABLE 2—*Continued*

Reference	W_λ(Ca II) (mÅ)	W_λ(Ca I) (mÅ)	W_λ(CH^+) (mÅ)	W_λ(CH) (mÅ)	W_λ(CN) (mÅ)
			HD 23568		
1	12.5 ± 1.0	≤1.6	18.4 ± 0.6	1.3 ± 0.4	≤3.3
2	15.6 ± 3.0	≤7.9	15.5 ± 2.6	≤7.7	≤8.7
			η Tau		
1	12.5 ± 0.4	≤0.4	2.0 ± 0.1	0.4 ± 0.1	≤0.9
2	15.0 ± 1.1	≤3.3	3.8 ± 0.7	≤2.8	≤3.7
5	12.1 ± 0.7	...	...	...	...
5	14.4 ± 1.2	...	...	...	...
6	11	...	...	...	...
7	...	...	1.7	...	...
9	...	...	1.6 ± 0.4	≤1.8	...
14	13.6 ± 0.2	...	...	...	...
15	8	≤0.64	...	...	...
			HD 23753		
1	11.0 ± 0.6	≤0.9	3.5 ± 0.2	≤0.7	≤1.2
2	10.6 ± 1.0	≤4.2	4.0 ± 0.9	≤4.5	≤5.5
4	...	...	7.6	...	...
			27 Tau		
1	17.7 ± 0.4	≤0.7	4.1 ± 0.3	0.4 ± 0.2	≤1.1
2	12.1 ± 1.2	≤3.9	5.0 ± 0.7	≤3.1	≤4.1
3	13 ± 1	...	≤13	≤13	...
6	12	...	...	...	...
7	...	...	4.2	...	...
			28 Tau		
1	17.0 ± 0.3	≤0.5	4.1 ± 0.2	0.6 ± 0.1	≤0.8
2	13.8 ± 1.6	≤4.5	≤2.9	≤3.5	≤5.1
			HD 23923		
1	12.7 ± 0.7	≤1.0	2.4 ± 0.3	≤0.8	≤1.4
2	16.9 ± 1.5	≤5.8	≤11	≤5.1	≤11

REFERENCES.—(1) This paper; (2) White 1984a; (3) Younan & Dufton 1984; (4) Frisch 1972; (5) Welty et al. 1996; (6) Marschall & Hobbs 1972; (7) Crane et al. 1995; (8) Hawkins & Jura 1987; (9) Federman 1982; (10) Vanden Bout & Snell 1980; (11) Hobbs 1973; (12) Vanden Bout & Thaddeus 1971; (13) Federman et al. 1994; (14) Vallerga et al. 1993; (15) White 1973.

widths and the parameters listed in Table 3. The adopted *b*-values, 1.6 km s^{-1} for Ca II, CH^+, and CH, and 0.5 km s^{-1} for CN, are average values for the respective species. However, most lines are weak so that measured equivalent widths for a given species fall on the linear portion of the curve of growth. Thus, the use of different *b*-values does not impact the derived column densities in any appreciable way. In particular, the largest optical depth at line center encountered under our assumptions is $\tau = 1.03$ for the $R(0)$ line of CN toward HD 23512. Table 4 summarizes our results for the individual components of Ca II K, CH^+, and CH, listing the column density, N, radial velocity, v_{LSR}, and *b*-value of each component. The reported uncertainty in N for a given component was inferred from the measured uncertainty in the value of W_λ. Table 4 also displays the relevant parameters of the components found by White et al. (2001) in their survey of interstellar Na I in the Pleiades. The last column gives the Na I/Ca II column density ratio, which is discussed further in § 4.2. For compactness, the CN column densities toward HD 23512 are not listed in Table 4 but are given here: $N(CN) = 2.7 \pm 0.3$, 1.6 ± 0.3, and ≤ 2.8 in units of 10^{12} cm^{-2} for the $R(0)$, $R(1)$, and

TABLE 3

WAVELENGTHS (AIR) AND *f*-VALUES

Species	λ_{air} (Å)	*f*-Value	Reference
Ca II	3933.663	0.6346	1
CH^+	4232.548	0.00545	2
CH	4300.313	0.00510	3
CN[a]	3874.00	0.0228	3
	3874.61	0.0342	3
	3875.76	0.0114	3

[a] First entry is for the $R(1)$ transition, second is for $R(0)$, and third is for $P(1)$.

REFERENCES.—(1) Morton 1991; (2) Gredel et al. 1993; (3) Federman et al. 1994.

TABLE 4

SUMMARY OF RESULTS FOR INDIVIDUAL COMPONENTS

Ca II			CH^+			CH			Na I[a]			
N (10^{10} cm^{-2})	v_{LSR} (km s^{-1})	b-Value (km s^{-1})	N (10^{12} cm^{-2})	v_{LSR} (km s^{-1})	b-Value (km s^{-1})	N (10^{12} cm^{-2})	v_{LSR} (km s^{-1})	b-Value (km s^{-1})	N (10^{11} cm^{-2})	v_{LSR} (km s^{-1})	b-Value (km s^{-1})	N(Na I)/N(Ca II)
					16 Tau							
1.8 ± 0.5.....	−8.2	1.9	≤1.8	...	...	≤1.2	...	...	≤0.9	...	...	≤5.0
4.6 ± 0.5.....	+5.1	1.4	≤1.8	...	...	0.6 ± 0.4	+6.6	1.6	2.8 ± 0.3	+6.4	1.3	6.1 ± 0.9
6.4 ± 0.5.....	+8.5	2.0	21.7 ± 0.6	+9.1	1.9	≤1.2	...	...	2.5 ± 0.3	+9.3	1.1	3.9 ± 0.6
					17 Tau							
0.8 ± 0.2.....	+3.3	0.4	≤0.6	...	...	≤0.7	...	...	≤0.2	...	...	≤2.5
4.3 ± 0.2.....	+6.7	1.4	0.9 ± 0.2	+7.5	1.6	≤0.7	...	...	2.0 ± 0.1	+7.0	1.1	4.6 ± 0.3
1.8 ± 0.4.....	+9.7	1.5	1.3 ± 0.2	+10.3	1.6	≤0.7	...	...	0.4 ± 0.1	+9.4	0.7	2.2 ± 0.7
0.8 ± 0.2.....	+14.0	1.3	≤0.6	...	...	≤0.7	...	...	≤0.2	...	...	≤2.5
					18 Tau							
1.9 ± 0.4.....	+4.3	1.6	≤1.2	...	...	≤1.0	...	...	≤0.4	...	...	≤2.1
9.8 ± 0.4.....	+6.7	1.6	≤1.2	...	...	≤1.0	...	...	3.6 ± 0.5	+7.4	1.0	3.7 ± 0.5
2.3 ± 0.4.....	+9.8	1.6	3.6 ± 0.4	+9.6	1.5	≤1.0	...	...	0.8 ± 0.1	+10.9	0.9	3.5 ± 0.7
					19 Tau							
1.5 ± 0.4.....	−5.8	1.8	≤0.6	...	...	≤0.6	...	...	≤3.0	...	...	≤20.0
3.4 ± 0.4.....	+5.7	1.6	3.3 ± 0.2	+6.9	1.8	≤0.6	...	...	4.0 ± 1.0	+6.7	1.0	11.8 ± 3.2
9.2 ± 0.4.....	+7.6	1.9	≤0.6	...	...	≤0.6	...	...	6.0 ± 1.1	+8.3	0.8	6.5 ± 1.2
					20 Tau							
9.3 ± 0.4.....	+6.6	1.7	15.7 ± 0.3	+7.2	1.5	≤0.8	...	...	8.0 ± 0.4	+6.9	1.0	8.6 ± 0.6
1.8 ± 0.2.....	+8.5	0.9	16.0 ± 0.3	+9.0	1.6	≤0.8	...	...	2.4 ± 0.2	+8.9	0.9	13.3 ± 1.8
					HD 23410							
2.8 ± 0.4.....	−5.3	0.9	≤1.2	...	...	≤1.2	...	...	0.6 ± 0.2	−5.2	0.2	2.1 ± 0.8
7.7 ± 0.5.....	+6.9	1.4	2.7 ± 0.4	+6.9	2.1	≤1.2	...	...	12. ± 0.8	+7.1	1.1	15.6 ± 1.4
					21 Tau							
3.8 ± 0.6.....	−5.9	1.6	≤2.1	...	...	≤1.3	...	...	≤1.9	...	...	≤5.0
6.8 ± 0.8.....	+5.9	2.2	4.9 ± 0.6	+7.0	2.3	≤1.3	...	...	4.1 ± 0.7	+6.9	1.0	6.0 ± 1.2
4.3 ± 0.6.....	+8.8	1.8	18.7 ± 0.8	+9.4	2.1	≤1.3	...	...	1.3 ± 0.6	+9.2	1.1	3.0 ± 1.4
					22 Tau							
1.3 ± 0.5.....	+3.5	1.4	≤1.8	...	...	≤1.1	...	...	≤1.4	...	...	≤10.8
5.9 ± 0.5.....	+6.4	1.4	≤1.8	...	...	≤1.1	...	...	4.0 ± 0.5	+6.8	1.0	6.8 ± 1.0
1.5 ± 0.4.....	+9.2	1.2	18.6 ± 0.6	+8.6	2.0	≤1.1	...	...	0.9 ± 0.4	+9.2	1.0	6.0 ± 3.1

TABLE 4—*Continued*

Ca II			CH^+			CH			Na I[a]			
N (10^{10} cm^{-2})	v_{LSR} (km s^{-1})	b-Value (km s^{-1})	N (10^{12} cm^{-2})	v_{LSR} (km s^{-1})	b-Value (km s^{-1})	N (10^{12} cm^{-2})	v_{LSR} (km s^{-1})	b-Value (km s^{-1})	N (10^{11} cm^{-2})	v_{LSR} (km s^{-1})	b-Value (km s^{-1})	N(Na I)/N(Ca II)
					23 Tau							
1.0 ± 0.2.....	−3.9	1.9	≤1.2	...	...	≤0.7	...	...	≤0.4	...	...	≤4.0
0.7 ± 0.2.....	+3.1	1.5	≤1.2	...	...	≤0.7	...	...	≤0.4	...	...	≤5.7
4.2 ± 0.2.....	+6.8	1.7	1.3 ± 0.4	+7.5	2.3	≤0.7	...	...	3.0 ± 0.5	+7.5	1.0, 3.4[b]	7.1 ± 1.2
3.8 ± 0.2.....	+9.4	1.6	18.4 ± 0.4	+10.2	2.2	≤0.7	...	...	1.0 ± 0.1	+10.6	0.6	2.6 ± 0.3
0.9 ± 0.2.....	+13.7	1.5	≤1.2	...	...	≤0.7	...	...	≤0.4	...	...	≤4.4
					HD 23512							
5.8 ± 1.5.....	+6.2	1.5	≤2.4	...	...	≤2.4	...	...	5.9 ± 3.1	+7.4	0.5	10.2 ± 6.0
7.8 ± 1.6.....	+9.2	1.6	6.2 ± 0.8	+9.1	1.7	5.4 ± 0.8	+9.8	1.6	>60.	+10.1	0.6	>76.9
					HD 23568							
6.3 ± 0.6.....	+5.5	1.6	≤3.0	...	...	≤1.5	...	...	≤2.5	...	...	≤4.0
6.3 ± 0.6.....	+7.6	1.8	≤3.0	...	...	1.6 ± 0.5	+7.5	1.6	9.4 ± 1.0	+7.1	1.0	14.9 ± 2.1
2.5 ± 0.8.....	+10.0	2.5	25.6 ± 1.0	+8.8	2.1	≤1.5	...	...	1.8 ± 0.6	+9.5	0.6	7.2 ± 3.3
					24 Tau							
1.2 ± 0.2.....	−3.7	...	≤0.6	...	...	≤0.8	...	...	≤2.0	...	...	≤16.7
3.1 ± 0.5.....	+4.3	1.4	≤0.6	...	...	≤0.8	...	...	≤2.0	...	...	≤6.4
11.1 ± 0.5.....	+7.2	1.5	2.5 ± 0.2	+7.6	1.0	≤0.8	...	...	9.7 ± 0.9	+7.1	2.6, 0.9[b]	8.7 ± 0.9
1.5 ± 0.4.....	+11.6	1.1	≤0.6	...	...	≤0.8	...	...	≤2.0	...	...	≤13.3
					η Tau							
2.0 ± 0.2.....	−4.2	1.2	≤0.3	...	...	≤0.3	...	...	0.1 ± 0.02	−3.4	1.9	0.5 ± 0.1
2.3 ± 0.2.....	+4.8	1.3	≤0.3	...	...	≤0.3	...	...	0.4 ± 0.05	+5.6	3.8	1.7 ± 0.3
9.7 ± 0.3.....	+7.2	1.3	2.4 ± 0.1	+7.2	1.4	0.5 ± 0.1	+6.0	1.5	7.5 ± 0.2	+7.5	1.1	7.7 ± 0.3
1.2 ± 0.2.....	+11.6	1.3	≤0.3	...	...	≤0.3	...	...	≤0.1	...	...	≤0.8
					HD 23753							
2.5 ± 0.5.....	+3.7	1.7	≤0.6	...	...	≤0.8	...	...	1.5 ± 0.2	+4.0	0.3	6.0 ± 1.4
9.2 ± 0.4.....	+7.3	1.2	4.2 ± 0.2	+8.1	1.7	≤0.8	...	...	7.2 ± 0.3	+7.6	1.2	7.8 ± 0.5
1.8 ± 0.5.....	+10.6	2.2	≤0.6	...	...	≤0.8	...	...	≤0.5	...	...	≤2.8
					27 Tau							
2.2 ± 0.2.....	−4.6	0.8	≤1.2	...	...	≤0.6	...	...	0.1 ± 0.01	−4.1	1.6	0.4 ± 0.1
0.9 ± 0.2.....	+4.3	1.4	≤1.2	...	...	≤0.6	...	...	≤0.03	...	...	≤0.3
17.7 ± 0.3.....	+7.1	1.3	4.9 ± 0.4	+7.2	2.1	0.5 ± 0.2	+7.2	1.6	20. ± 1.1	+7.2	3.8, 0.9[b]	11.3 ± 0.6
1.9 ± 0.2.....	+11.0	1.8	≤1.2	...	...	≤0.6	...	...	0.7 ± 0.2	+9.0	0.6	3.7 ± 1.1

TABLE 4—*Continued*

Ca II			CH^+			CH			Na I[a]			
N (10^{10} cm^{-2})	v_{LSR} (km s^{-1})	b-Value (km s^{-1})	N (10^{12} cm^{-2})	v_{LSR} (km s^{-1})	b-Value (km s^{-1})	N (10^{12} cm^{-2})	v_{LSR} (km s^{-1})	b-Value (km s^{-1})	N (10^{11} cm^{-2})	v_{LSR} (km s^{-1})	b-Value (km s^{-1})	N(Na I)/N(Ca II)
					28 Tau							
2.0 ± 0.1.....	−4.5	1.0	≤0.6	...	...	≤0.3	...	...	≤0.6	...	...	≤3.0
0.7 ± 0.1.....	+4.0	1.2	≤0.6	...	...	≤0.3	...	...	≤0.6	...	...	≤8.6
17.9 ± 0.3.....	+7.3	1.4	4.9 ± 0.2	+7.4	2.0	0.7 ± 0.1	+7.4	1.6	4.7 ± 0.2	+6.8	1.0	2.6 ± 0.1
1.4 ± 0.2.....	+11.5	2.1	≤0.6	...	...	≤0.3	...	...	≤0.6	...	...	≤4.3
					HD 23873							
16.2 ± 1.0.....	+5.8	1.8	≤2.1	...	...	≤1.2	...	...	7.9 ± 0.3	+6.6	1.5	4.9 ± 0.4
5.0 ± 0.7.....	+8.1	1.6	4.4 ± 0.7	+7.7	2.1	≤1.2	...	...	≤1.0	...	...	≤2.0
2.5 ± 0.6.....	+12.2	1.1	≤2.1	...	...	≤1.2	...	...	≤1.0	...	...	≤4.0
					HD 23923							
2.9 ± 0.4.....	+3.2	1.1	≤1.2	...	...	≤1.0	...	...	3.0 ± 0.2	+3.9	1.5	10.3 ± 1.6
10.9 ± 0.4.....	+6.8	1.6	2.8 ± 0.4	+6.5	1.5	≤1.0	...	...	6.8 ± 0.4	+7.1	0.8	6.2 ± 0.4
1.8 ± 0.6.....	+12.6	2.3	≤1.2	...	...	≤1.0	...	...	≤1.0	...	...	≤5.6
					HD 23964							
4.9 ± 0.7.....	−3.7	1.8	≤1.3	...	...	≤1.5	...	...	0.3 ± 0.04	−3.7	0.5	0.6 ±0.1
2.6 ± 0.6.....	+3.3	1.5	≤1.3	...	...	≤1.5	...	...	3.1 ± 0.8	+4.8	2.7	11.9 ± 4.1
9.0 ± 0.5.....	+6.2	1.3	≤1.3	...	...	≤1.5	...	...	7.5 ± 0.8	+6.7	1.1	8.3 ± 1.0
2.0 ± 0.4.....	+9.4	0.4	≤1.3	...	...	≤1.5	...	...	≤1.0	...	...	≤5.0
0.9 ± 0.2.....	+12.0	...	≤1.3	...	...	≤1.5	...	...	≤1.0	...	...	≤11.1
					HD 24076							
1.4 ± 0.7.....	+5.0	1.8	≤2.1	...	...	≤1.3	...	...	≤1.7	...	...	≤12.1
8.6 ± 0.8.....	+7.2	1.6	4.7 ± 0.7	+7.5	2.2	≤1.3	...	...	9.7 ± 0.6	+6.9	1.1	11.3 ± 1.3

[a] From White et al. (2001).
[b] Column densities of very closely spaced Na I components were summed for comparison purposes. The velocity stated for summed components is a weighted average; however, both b-values are listed.

TABLE 5
Mean Velocities and Doppler Parameters

Species	Stars	Components	$\langle v_{LSR} \rangle$ (km s^{-1})	$\langle b \rangle$ (km s^{-1})
Ca II[a]	20	65	+6.2	1.5 ± 0.4
	20	55	+7.1	1.5 ± 0.4
CH^+	19	23	+8.6	1.8 ± 0.3
CH	6	6	+8.7	1.6 ± 0.1
CN	1	1	+9.4	0.5 ± 0.1
Na I[b]	20	42	+7.9	1.2 ± 0.8
	20	37	+8.0	1.0 ± 0.3

[a] Second row is for positive velocity Ca II components only.
[b] From White et al. (2001). The second row excludes five broad Na I components with $b > 2.5$ km s^{-1}.

$P(1)$ lines, respectively. These quantities will be important later for deriving the density of the molecular cloud along this line of sight.

3.3. *Doppler Parameters and Radial Velocities*

The mean and dispersion in b-values were calculated for the detected species of this survey as well as for Na I from the data provided by White et al. (2001). The results are displayed in Table 5. To facilitate a meaningful comparison, the values in the last row of the table were calculated by excluding five broad Na I components with $b > 2.5$ km s^{-1}. The scatter in b-values for the species in our investigation is low and is comparable to the scatter found for the narrow Na I components. Our mean b-values show good agreement with those from previous investigations, both within the Pleiades and in other regions of the ISM, for which spectra of comparable S/N were acquired. The ultra–high-resolution survey of CH^+ and CH by Crane et al. (1995), for instance, included four Pleiades stars: 20 Tau, 23 Tau, η Tau, and 27 Tau. While they did not claim to detect CH along these sight lines, their mean CH^+ b-value for the four stars (1.9 ± 0.5 km s^{-1}) agrees closely with the mean value for our sample of 19 sight lines (1.8 ± 0.3 km s^{-1}). Welty et al. (1996) observed two Pleiades stars, 17 Tau and η Tau, in a high-resolution survey of Ca II. Their average b-value for the six components detected toward these two stars (1.5 ± 0.9 km s^{-1}) is identical to our average for 20 stars (1.5 ± 0.4 km s^{-1}), although the median value for their entire sample is somewhat smaller (∼1.3 km s^{-1}). Pan et al. (2005) measured average b-values for a number of atomic and molecular species in an extensive examination of interstellar absorption in three star-forming regions: ρ Oph, Cep OB2, and Cep OB3. Based on detections of 350 total components for Ca II and over 100 components for the other species excluding CN, for which they detect 50 components, these authors found average b-values of 1.62 ± 0.28 km s^{-1} for Ca II, 1.96 ± 0.23 km s^{-1} for CH^+, 1.04 ± 0.18 km s^{-1} for CH, and 0.83 ± 0.11 km s^{-1} for CN. Given the uncertainties, the mean b-values in Table 5 are consistent with these results, except in the case of CH. The larger value we obtain for this species (1.6 ± 0.1 km s^{-1}) may have implications for the environment responsible for the formation of these lines.

Previous studies have shown that CH can exist in both low-density gas ($n \sim 100$ cm^{-3}), where it is produced via nonthermal CH^+ chemistry (Draine & Katz 1986; Zsargó & Federman 2003), and in higher density regions ($n \sim 600$ cm^{-3}) where CN resides (Federman et al. 1994). CH components associated with CH^+ can be identified by a broad "CH^+-like" absorption profile, whereas those found in regions where CN is detected will exhibit a sharper "CN-like" profile (Lambert et al. 1990). In the analysis of Pan et al. (2005), CN-like CH components were discovered to have an average b-value indistinguishable from that of CN components (0.90 ± 0.11 km s^{-1}), while CH^+-like CH components had a larger average b-value (1.10 ± 0.16 km s^{-1}). The CH components examined in the Pleiades are more closely associated with CH^+ than along average sight lines. Indeed, our mean CH b-value is nearly indistinguishable from our mean value for CH^+ and well above the b-values of the only detected CN lines [0.5 and 0.6 km s^{-1} for $R(0)$ and $R(1)$, respectively, toward HD 23512]. Toward most of the Pleiades, therefore, CH is found to be CH^+-like as opposed to CN-like. That is, CH is linked to the formation of CH^+ rather than CN and traces lower density interstellar clouds. This conclusion would not be altered had we considered Λ-doubling in the CH line, which would lower our CH b-values by ∼0.2 km s^{-1}.

Table 5 also presents the mean radial velocities of the various species weighted by the column density of each component. These quantities yield information on the bulk kinematic properties of the various constituents of the interstellar gas near the Pleiades. The column density weighted mean velocity for Ca II in our sample is ∼+6 km s^{-1}, whereas for molecular species this average is closer to ∼+9 km s^{-1}. If only positive Ca II velocity components are included, the mean velocity increases to ∼+7 km s^{-1}. White (1984a) was the first to note the kinematic separation of atomic and molecular gas in this cluster. His results yielded average velocities of ∼+7 km s^{-1} for Ca II and ∼+8 km s^{-1} for CH^+. The distinction may be even more pronounced in the average velocities reported here, especially considering our measurements of CH and CN velocities. The Na I components (White et al. 2001) have a weighted mean velocity of ∼+8 km s^{-1} in somewhat closer agreement with the molecular species than with Ca II, suggesting that ionized and neutral gas may also be kinematically distinct. In § 4 the bulk motions described above are examined in greater detail by identifying individual velocity components present in the atomic and molecular gas.

4. DATA ANALYSIS

4.1. *Velocity Components*

In order to analyze the complex interactions between the interstellar gas and the stars of the Pleiades and to attempt to map the extent of the clouds involved in these interactions, contour maps were generated showing the spatial distribution of individual velocity components for species with detectable absorption along more than one line of sight. These maps are presented in Figures 6–8 for CH, CH^+, and Ca II in order of increasing complexity. The contours in these figures were drawn by eye to include all sight lines that exhibit a given component. However, since we only have information at a limited number of discrete points, unlike radio data, for instance, the boundaries shown are approximate at best. As a rule, if a component was found along one sight line but not along another adjacent to it, a boundary was drawn halfway between. When no sight line was available to constrain the outer portions of a given component, contours were drawn to the edge of the plot.

4.1.1. CH *and* CH^+ *Velocity Components*

For the molecular species, CH and CH^+, one component was typically found per absorbing sight line, falling in either of two categories, those with $v_{LSR} \sim +7$ km s^{-1} and those with $v_{LSR} \sim +9.5$ km s^{-1}. The former correspond to the "central" component in the Na I profiles analyzed by White (2003), who identified

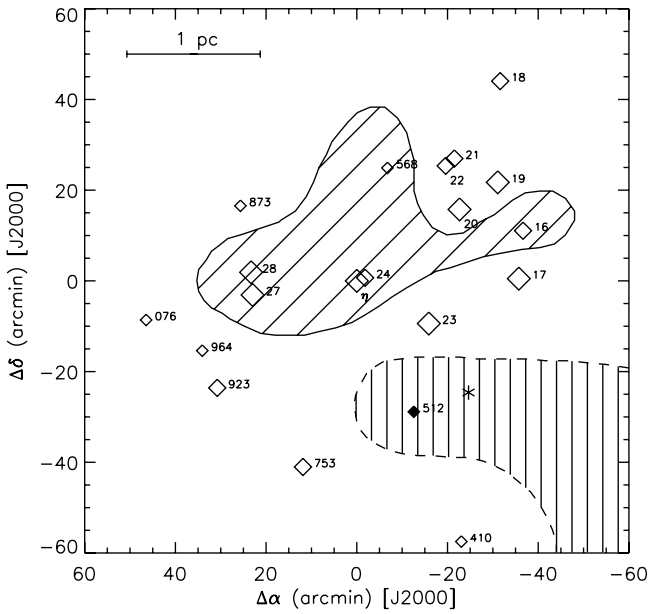

FIG. 6.—Contour plot of the observed velocity components of CH mapped onto the stars of the Pleiades. Filled symbols denote the strongest absorption components. The region enclosed by the solid line (*diagonal hatching*) has a velocity range (in kilometers per second) of $+6.0 \leq v_{\rm LSR} \leq +7.5$, and the star enclosed by the dashed line (*vertical hatching*) has a velocity of +9.8 km s^{-1}. Although no component is detected toward 24 Tau, this star is included within the central contour because its column density upper limit of $\lesssim 0.8 \times 10^{12}$ cm^{-2} is consistent with a detection comparable in size to that found toward its binary companion, η Tau, for which $N = 0.5 \times 10^{12}$ cm^{-2}. The asterisk marks the position of peak CO emission from the molecular cloud discussed in the text.

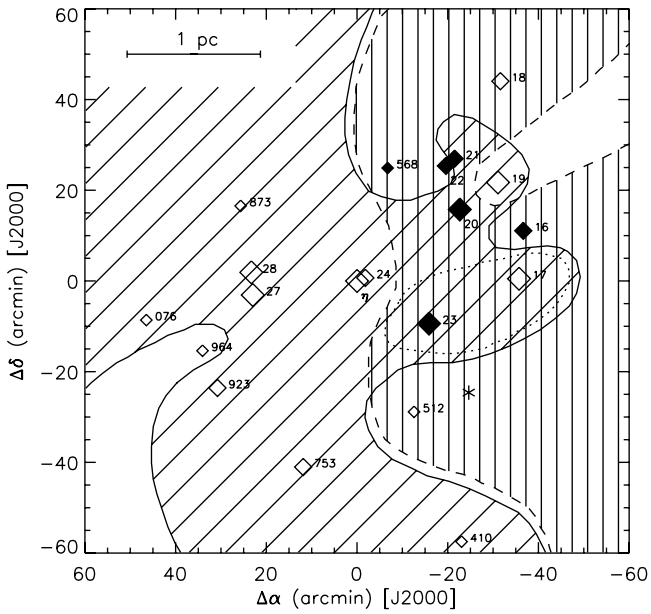

FIG. 7.—Contour plot of the observed velocity components of CH^+ mapped onto the stars of the Pleiades. Filled symbols denote the strongest absorption components. The area between the solid lines (*diagonal hatching*) has a velocity range (in kilometers per second) of $+6.5 \leq v_{\rm LSR} \leq +8.1$, and between the dashed lines (*vertical hatching*) has a velocity range of $+8.6 \leq v_{\rm LSR} \leq +10.3$. The two sight lines enclosed by the dotted line have velocities of +10.2 and +10.3 km s^{-1}. Again, the asterisk marks the position of peak CO emission from the molecular cloud.

this absorption with the pervasive foreground gas thought to be associated with the Taurus dust clouds (see also White & Bally 1993). The latter, also detected in the Na I data, were termed the "red" component by White (2003), who suggested that this is either Taurus gas redshifted to higher radial velocities by the interaction with cluster stars or an independent gas cloud also interacting with the Pleiades. In our data, the strongest molecular absorption, including the only absorption detected in CN, is associated with the higher velocity component. The lower velocity gas is more pervasive, and the two components generally occupy different regions of the cluster.

Figure 6 clearly illustrates the spatial distinction between 7 and 9.5 km s^{-1} gas in the velocity components of CH and demonstrates the trend in absorption strength as well. There are five weak components with a mean velocity of +6.9 km s^{-1} concentrated in the central region of the cluster. Four of these have column densities below 1×10^{12} cm^{-2}, and the fifth, toward HD 23568, has a column density of 1.6×10^{12} cm^{-2}. A much stronger component, with $N = 5.4 \times 10^{12}$ cm^{-2}, is detected at a velocity of +9.8 km s^{-1} toward HD 23512. The sight line to HD 23512 passes through a small molecular cloud first mapped in CO emission by R. S. Cohen (1975, unpublished; see Federman & Willson 1984). The asterisk in Figure 6 marks the position of peak CO emission from the cloud. Federman & Willson published Cohen's CO data and added additional radio observations of CO and ^{13}CO, as well as CH and OH, determining the velocity of the cloud to be about 10 km s^{-1}. Our velocity for the CH component toward HD 23512 is consistent with their determination. In addition, the $R(0)$ and $R(1)$ lines of CN detected toward this star give velocities of +9.4 and +9.5 km s^{-1}, respectively. CN traces dense clouds, and the extensive study by Pan et al. (2005) found that strong CH absorption is associated with CN (see § 3.3). Thus, it is not surprising that CN is only found along a sight line containing a molecular cloud and that the CN-like CH component in this direction has a consistent velocity.

Although the CH^+ components in Figure 7 exhibit more complexity in their spatial distribution, the general trends are still apparent. Fourteen components are detected at a mean velocity of +7.3 km s^{-1}. These are distributed in mainly the central and eastern parts of the cluster, with some components extending to the south and to the west. The majority have column densities of $\sim(3\text{–}5) \times 10^{12}$ cm^{-2}. The higher velocity components responsible for the largest column densities of CH^+ are concentrated in the western half of the cluster. Nine components are found at a mean velocity of +9.3 km s^{-1}, and six of these have column densities greater than 15×10^{12} cm^{-2}. The components toward 17 Tau and 23 Tau have the highest velocities of this group, +10.3 and +10.2 km s^{-1}, respectively, noticeably higher than the velocity of any other component. These velocities coincide with the velocity of the molecular cloud discussed above, and the sight lines toward these stars lie along the cloud's outer edge as seen in molecular emission (Federman & Willson 1984). Both are strong indications that the material responsible for the absorption originated in the molecular cloud. Interestingly, no 7 km s^{-1} gas is detected in the cloud's immediate vicinity (toward HD 23512) but is seen in weak absorption to the north (toward 17 Tau and 23 Tau) and in more moderate absorption to the south (toward HD 23410). We do not detect any systematic velocity shifts between our CH and CH^+ lines. The average difference in velocity for components detected in both species is $v(CH^+) - v(CH) = 0.1$ km s^{-1}. Our CH velocities also agree well with those of Na I, with an average difference for individual sight lines of $v(CH) - v(\text{Na I}) = -0.1$ km s^{-1}.

4.1.2. Ca II *Velocity Components*

While the molecular data can be adequately represented by two distinct velocity components, the situation for Ca II is considerably

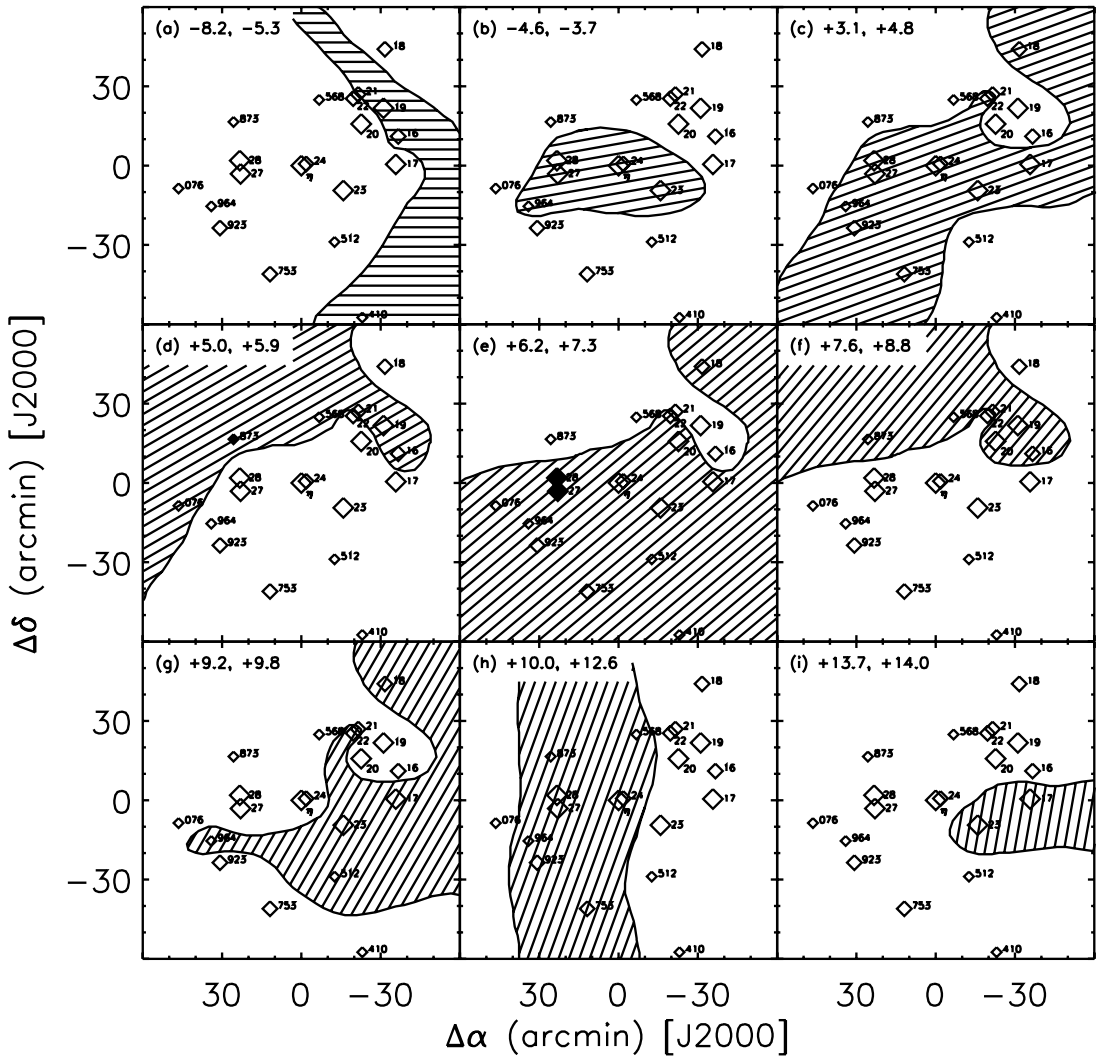

FIG. 8.—Contour plots of the observed velocity components of Ca II mapped onto the stars of the Pleiades. Filled symbols denote the strongest absorption components. The minimum and maximum velocities (in kilometers per second) for each panel are labeled.

more complex. Up to five separate components are identified along a single line of sight. In all, 55 components are detected with velocities distributed almost continuously from +3.1 to +14.0 km s^{-1}. Another 10 are found with velocities between −8.2 and −3.7 km s^{-1}. Velocities alone are not enough to categorize components with such diversity. Thus, the panels displayed in Figure 8 were created by classifying the Ca II components not only according to their velocity, but also to their proximity to like sight lines and their overall position in the cluster. The notable features of this figure are as follows.

The most pervasive group of Ca II components (Fig. 8*e*) has a mean velocity of +6.8 km s^{-1}, clearly associating it with the central component of White's (2003) analysis and that found in our molecular data. This component pervades the observed extent of the cluster with the exception of five sight lines along the northern edge: 16 Tau, 19 Tau, 21 Tau, HD 23568, and HD 23873. Unlike the weaker molecular feature at this velocity, the central Ca II component is the dominant source of atomic absorption in the Pleiades, with column densities in the range $(4–18) \times 10^{10}$ cm^{-2}. Proceeding outward in velocity from the central component, there are two groups (Figs. 8*d* and 8*f*) that appear nearly identical in their morphology and spatial extent. These groups have mean velocities of +5.5 and +8.2 km s^{-1}, respectively, and seem to populate the apparent void in the central component. Indeed, all five of the aforementioned northern sight lines have components at both the slightly higher and slightly lower velocities. We interpret this bifurcation in velocity components, which appears smooth at our resolution, as evidence of a velocity gradient in the pervasive central cloud. However, the number of components belonging to groups 8*d* and 8*f* may be complicated by unresolved component blending in the central component (Fig. 8*e*). For example, Welty et al. (1996) fitted the asymmetric central region of their higher resolution Ca II profile toward η Tau with two components with velocities of +6.2 and +7.7 km s^{-1}, compared to our one component with a velocity of +7.2 km s^{-1}. In our data, a hint of this asymmetry in the central region of the profile can be seen for η Tau, as well as for 27 Tau and 28 Tau. In general, however, the *b*-values for these three groups of Ca II components are quite similar ($\sim$1.6 km s^{-1}) and thus do not indicate that unresolved structure is a major concern.

Moving out still farther in velocity from the central component, we encounter two additional groups (Figs. 8*c* and 8*g*) with analogous spatial characteristics. These groups, with mean velocities of +3.8 and +9.4 km s^{-1}, respectively, exhibit identical structure in the cluster's northwest quadrant, but the lower velocity components (Fig. 8*c*) are more extensive in the southeast. Interestingly, the six sight lines that are missing from the feature in Figure 8*g* have components at even higher velocities (Fig. 8*h*).

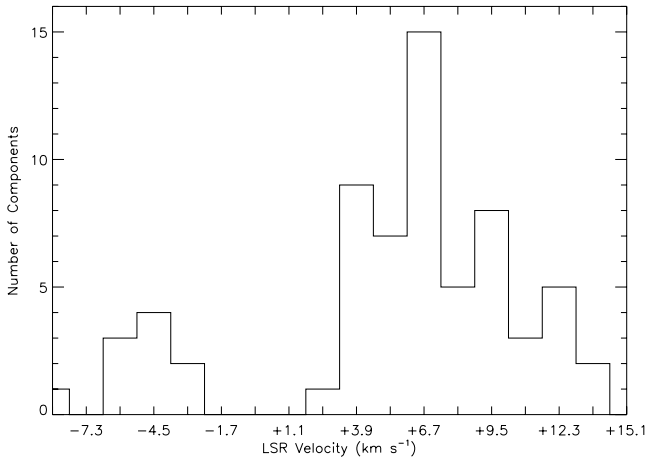

FIG. 9.—Representative histogram of Ca II velocity components with a bin size of 1.4 km s^{-1}, comparable to our velocity resolution.

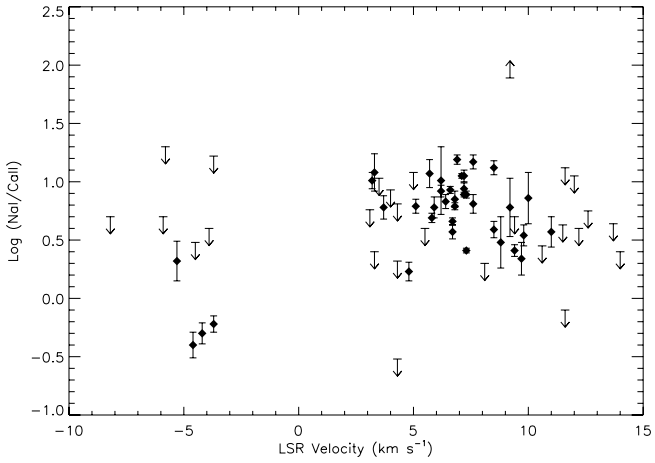

FIG. 10.—N(Na I)/N(Ca II) ratios as a function of v(Ca II). Of the four data points with $v_{LSR} < 0$, three have ratios less than 1. These are for the shocked components toward η Tau, 27 Tau, and HD 23964. The fourth, with a ratio of ~2, is for the shocked component toward HD 23410. The lower limit near the top of the figure is for the +9.2 km s^{-1} component toward HD 23512.

This group (Fig. 8*h*) has a mean velocity of +11.5 km s^{-1}. Taken together, the components in Figures 8*g* and 8*h* are roughly comparable to the red component in White's (2003) classification scheme. Those in Figure 8*c* correspond to what White (2003) termed the "blue" component, with the implication that gas from the central cloud at $v_{LSR} \sim +7$ km s^{-1} has been blueshifted by its interaction with the cluster to lower radial velocities. The spatial correlations and morphological similarities of redshifted and corresponding blueshifted components in Figure 8 are striking and support the claim that velocity gradients reflect the interaction on a cloud. Furthermore, the mean velocities found for the components of Figures 8*c* and 8*g* differ from the mean velocities of the previous two groups (Figs. 8*d* and 8*f*) by an amount consistent with the velocity differences between those groups and the central component. In other words, Figures 8*c*–8*g* present successive velocity intervals of approximately 1.4 km s^{-1}, evincing the symmetry of the interstellar gas in the Pleiades traced by Ca II absorption.

The remaining panels of Figure 8 present further components that do not conform to the above symmetries. The components with the most extreme positive velocities (Fig. 8*i*) inhabit a region directly west of the cluster center. It is notable that the two sight lines showing this component, 17 Tau and 23 Tau with velocities of +14.0 and +13.7 km s^{-1}, respectively, are the same as those with the highest CH^+ velocities, although the actual velocities do not agree. The proximity of these highly redshifted components to the edge of the molecular cloud is suggestive of strong interactions between cloud material and the luminous blue giants. Figures 8*a* and 8*b* reveal the distribution of Ca II absorption detected at negative velocities. The six components concentrated in the central region of the cluster (Fig. 8*b*) have a mean velocity of −4.1 km s^{-1}, in close agreement with the negative-velocity components found in Na I. White (2003) named this the "shocked" component, referring to the prediction that strongly blueshifted absorption features would arise in foreground gas shocked by the interaction with cluster stars. Four additional shocked components are detected along the cluster's western edge (Fig. 8*a*). These have even more strongly blueshifted velocities with a mean of −6.3 km s^{-1}. White found shocked Na I components toward only HD 23410, η Tau, 27 Tau, and HD 23964, yet hinted at unpublished Ca II data confirming additional detections toward 21 Tau and 28 Tau. We also detect shocked Ca II components toward 21 Tau and 28 Tau, and add to this list 16 Tau, 19 Tau, 23 Tau, and 24 Tau. The shocked atomic components provide an important observational constraint when considering the types of interactions needed to explain the features of the ISM in the Pleiades.

We performed a statistical analysis to determine whether binning the Ca II velocity components in Figure 8 differently would severely alter our results. To this end, a series of histograms were constructed with successive bin sizes from 0.2 to 1.9 km s^{-1}. In almost every case, four distinct peaks could be seen for the positive-velocity components, with another single peak evident for the components with negative velocity. A representative histogram is shown in Figure 9 with a bin size of 1.4 km s^{-1}, comparable to the resolution in our data. The peaks in the figure are centered about values of −4.5, +3.9, +6.7, +9.5, and +12.3 km s^{-1}, closely echoing the mean velocities found for the components in Figures 8*b*, 8*c*, 8*e*, 8*g*, and 8*h*, respectively. Because variations in bin size have a negligible effect on the results presented in Figure 8, these features are not an artifact of a particular classification scheme, but represent physical structure in the interstellar atomic gas.

4.2. Na I/Ca II *Column Density Ratios*

The last column of Table 4 displays the N(Na I)/N(Ca II) ratios for our Ca II components common to the Na I investigation of White et al. (2001) and upper limits for Ca II components not detected in Na I. Figure 10 plots these ratios as a function of v(Ca II). Routly & Spitzer (1952) were the first to demonstrate that the Na I/Ca II column density ratios are inversely proportional to the velocity of the material. This phenomenon, known as the Routly-Spitzer effect, was later confirmed by Siluk & Silk (1974), who found that the decrease in N(Na I)/N(Ca II) was most evident for components with absolute velocities greater than ~20 km s^{-1}. The Routly-Spitzer effect is generally attributed to variations in the gas-phase abundance of calcium in clouds at different velocities. Calcium is depleted onto the surfaces of dust grains in low-velocity diffuse interstellar clouds resulting in high Na I/Ca II ratios in these environments. Heating from shock waves and cloud collisions in higher velocity material can cause grain destruction, which releases calcium back to its gaseous phase, yielding a lower Na I/Ca II ratio. The data in Figure 10 show an indication of this trend, but there are not enough high-velocity detections to be certain.

More importantly, because calcium depletion is assumed to be density dependent, our Na I/Ca II ratios can be used to characterize

the physical conditions of the interstellar clouds responsible for the detected absorption, providing a test for our derived column densities. The majority of positive-velocity components in Figure 10 have N(Na I)/N(Ca II) of order a few to 10, consistent with the values typical of diffuse, nonmolecular clouds with densities of $\sim$10 cm^{-3} (Hobbs 1976). The only exception to this is the +9.2 km s^{-1} component toward HD 23512. The Na I/Ca II ratio for this component (the lower limit near the top of Fig. 10) is of order 100, more characteristic of a denser, molecular cloud where calcium is depleted onto grain surfaces more effectively (Crawford et al. 1989; Crawford 1992). In contrast, the +6.2 km s^{-1} component along this sight line has a ratio of $\sim$10, placing it among the diffuse components where calcium depletion is less severe. Since these results predict the proper relationship between velocity components and the expected physical characteristics of the associated clouds, it gives us confidence in the accuracy of our derived column densities. A conspicuous feature of Figure 10 is that the Na I/Ca II ratios for shocked atomic components (those with $v_{\rm LSR} < 0$) are less than 1 except toward HD 23410, for which N (Na I)/N(Ca II) $\sim$ 2. In the environment near the Pleiades, a ratio less than 1 probably implies that photoionization from bright cluster stars has led to a reduction in neutral sodium. This effect would be less pronounced for gas near HD 23410 lying far from the more luminous stars and producing little luminosity of its own. The shocks themselves do not have high enough velocities to contribute much gas-phase calcium from grain processing.

4.3. *Physical Conditions*

It is possible to extract the physical conditions of the ISM near the Pleiades directly from our absorption-line data. In this section, we derive estimates for n, the total gas density of the absorbing clouds, and $I_{\rm UV}$, the enhancement of the UV radiation field due to cluster stars over the average Galactic field, by adopting various models of diffuse cloud chemistry.

4.3.1. *Steady State Model of* CH *Formation from* CH^+

For the majority of sight lines in our sample, CH is found to be closely associated with CH^+. In such environments, the total gas density, defined as $n = n(\mathrm{H}) + 2n(\mathrm{H_2})$, may be obtained by studying the reactions that lead to the production of CH from CH^+. In the calculations that follow, we do not explicitly consider the factors responsible for CH^+ formation. Instead, we follow the chemistry once CH^+ is present in appreciable amounts. In particular, we use the observed column density of CH^+ to determine the gas density implied by the amount of CH present. Assuming that the most important reactions,

$$\mathrm{CH^+ + H_2 \rightarrow CH_2^+ + H},$$
$$\mathrm{CH_2^+ + H_2 \rightarrow CH_3^+ + H},$$
$$\mathrm{CH_3^+ + \mathit{e} \rightarrow CH + H_2 \ or \ 2H},$$

satisfy the conditions for a steady state, the rate equation for CH may be written (Welty et al. 2006)

$$N(\mathrm{CH}) = \frac{0.67k(\mathrm{CH^+},\ \mathrm{H_2})N(\mathrm{CH^+})f(\mathrm{H_2})n}{2I_{\rm UV}G(\mathrm{CH})}, \qquad (1)$$

where the factor 0.67 represents the fraction of dissociative recombinations of CH_3^+ producing CH (Herbst 1978; Vejby-Christensen et al. 1997), $k(\mathrm{CH^+},\ \mathrm{H_2}) = 1.2 \times 10^{-9}$ cm^3 s^{-1} is the rate coefficient for the initial reaction (Draine & Katz 1986), $f(\mathrm{H_2}) = 2N(\mathrm{H_2})/N_{\rm tot}(\mathrm{H})$ is the fraction of hydrogen in molecular form, and $G(\mathrm{CH}) = 1.3 \times 10^{-9}\ e^{-\tau_{\rm UV}}$ s^{-1} is the CH photodissociation rate for the average Galactic field (Federman & Huntress 1989). In the expression for $f(\mathrm{H_2})$, $N_{\rm tot}(\mathrm{H}) = N(\mathrm{H\ I}) + 2N(\mathrm{H_2})$ denotes the total hydrogen column density along the line of sight. Equation (1) may be inverted to derive an expression for the gas density as a function of the CH/CH^+ column density ratio,

$$n = \frac{N(\mathrm{CH})}{N(\mathrm{CH^+})}\,\frac{2I_{\rm UV}G(\mathrm{CH})}{0.67k(\mathrm{CH^+},\ \mathrm{H_2})f(\mathrm{H_2})}. \qquad (2)$$

To estimate the gas density from equation (2), a few important parameters must first be determined, namely $f(\mathrm{H_2})$ and $I_{\rm UV}$. The first of these, the molecular fraction, is not well constrained in the vicinity of the Pleiades due to a dearth of reliable measurements of N(H I). As a starting point in our analysis, we adopted a value of $f(\mathrm{H_2}) = 0.1$ due to the strong presence of CH^+ in these clouds. A greater fraction of hydrogen in molecular form would rapidly destroy CH^+ by the reaction $\mathrm{CH^+ + H_2 \rightarrow CH_2^+ + H}$. Since n is inversely proportional to f, a lower value of f would increase the densities obtained from equation (2), a fact that is exploited in § 4.3.2. Individual values of $I_{\rm UV}$ are calculated using the following expression modified from equation (2) of White (1984b),

$$I_{\rm UV} = \left[1 + \frac{\chi_\lambda(1)}{x^2}\right] e^{-\tau_{\rm UV}} + \chi_{\lambda,c}, \qquad (3)$$

where $\chi_\lambda(1)$ is the ratio of the flux due to a specific star at a distance of 1 pc to that produced by the unattenuated galactic background, $\chi_{\lambda,c}$ is the corresponding ratio for the flux due to the other cluster stars at that position, and x is the distance from the star in parsecs. The radiative parameters for 14 of our 20 stars (at $\lambda = 1000$ Å) are obtained from Table 1 of White (1984b), from which x is taken to be $x_{\rm min}$, which is the minimum distance at which radiation pressure is balanced by the drag force on dust grains slipping through the gas as it approaches the cluster. Yet, since x in equation (3) refers to the gas responsible for the absorption, the adoption of these values assumes a close coupling between the gas and dust, although the actual distances used ($x \sim 0.1$–0.4 pc) are quite similar to those found in other analyses. For example, Jura (1977) argued for a distance of 0.1 pc for the gas toward 20 Tau, and Federman (1982) determined the distance to be 0.3 pc. The value obtained from White (1984b) for the gas toward this star is also 0.3 pc. Finally, to calculate $I_{\rm UV}$ as well as G(CH), we approximate $\tau_{\rm UV}$, the grain optical depth at 1000 Å, by $2A_V$ (Federman et al. 1994), determined from the reddening values in Table 1.

Table 6 displays the relevant parameters for each sight line and the resulting density estimates. Because the majority of sight lines show no detectable CH absorption, most of the densities in column (5) are only upper limits. We do not attempt to apply this method to the sight line toward HD 23512 because the assumptions leading to equation (2) would not be appropriate for the gas in a molecular cloud where CH is linked to CN chemistry. Of the remaining five sight lines with both CH^+ and CH in detectable amounts, two (16 Tau and HD 23568) do not have components at similar velocities. Thus, only three actual estimates for density can be obtained from our data using this procedure. The values, $n = 46$, 16, and 40 cm^{-3} for the sight lines toward η Tau, 27 Tau, and 28 Tau, respectively, are significantly below the densities predicted by earlier investigations. The atomic ionization models of White (1984a) favored a density of 400 cm^{-3}, while his chemical models of CH and CH^+ commonly employed values of 100 and 300 cm^{-3} (White 1984b). The 21 cm data examined by Gordon & Arny (1984) also suggested a hydrogen density of $\sim$100 cm^{-3}. However, a recent analysis by Zsargó

TABLE 6
PHYSICAL CONDITIONS

	FROM CH/CH$^+$ COLUMN DENSITY RATIO				FROM H_2 COLUMN DENSITIES				
STAR (1)	τ_{UV} (2)	$N(CH)/N(CH^+)$ (3)	I_{UV}[a] (4)	n[b] (cm^{-3}) (5)	$N(J=0)$[c] (10^{19} cm^{-2}) (6)	$N(J=1)$[c] (10^{19} cm^{-2}) (7)	$N(J=4)$[d] (10^{15} cm^{-2}) (8)	n[e] (cm^{-3}) (9)	I_{UV}[f] (10)
16 Tau	0.62	≥0.3	28.9	≥168	...	...	...	...	...
	...	≤0.06	...	≤28	...	...	...	...	...
17 Tau	0.31	≤0.8	21.9	≤404	...	...	...	...	...
	...	≤0.5	...	≤280	...	...	...	...	...
18 Tau	0.31	≤0.3	13.3	≤88	...	...	...	...	...
19 Tau	0.25	≤0.2	34.5	≤158	...	...	...	...	...
20 Tau	0.43	≤0.05	14.9	≤16	2.4 ± 1.0	3.2 ± 1.3	1.3 ± 0.2	89 ± 34	8.6 ± 3.4
	...	≤0.05	...	≤16	...	...	...	...	...
21 Tau	0.43	≤0.3	14.7	≤82	...	...	...	...	...
	...	≤0.07	...	≤21	...	...	...	...	...
22 Tau	0.37	≤0.06	7.9	≤10	...	...	...	...	...
23 Tau	0.62	≤0.5	20.5	≤192	7.8 ± 2.0	5.2 ± 1.3	2.2 ± 0.2	48 ± 12	7.1 ± 1.8
	...	≤0.04	...	≤14	...	...	...	...	...
HD 23568	0.43	≥0.5	6.4	≥72	...	...	...	...	...
	...	≤0.06	...	≤8	...	...	...	...	...
η Tau	0.25	0.2	8.8	46 ± 9	1.6 ± 0.4	1.9 ± 0.5	0.8 ± 0.1	83 ± 20	6.3 ± 1.6
HD 23753	0.25	≤0.2	11.0	≤53	...	...	...	...	...
27 Tau	0.25	0.1	6.1	16 ± 6	...	...	...	...	...
28 Tau	0.19	0.1	10.3	40 ± 6	...	...	...	...	...
HD 23923	0.37	≤0.4	3.6	≤29	...	...	...	...	...

[a] UV flux calculated from parameters in White (1984b).
[b] Gas density calculated from parameters in cols. (2)–(4). Two entries indicate multiple components along the line of sight.
[c] H_2 column densities from Savage et al. (1977).
[d] H_2 column density from Spitzer et al. (1974) for 20 Tau, and from Frisch & Jura (1980) for 23 and η Tau.
[e] Gas density calculated from parameters in cols. (6)–(8).
[f] UV flux calculated from parameters in cols. (6)–(8).

& Federman (2003) of C I excitation yielded a gas density upper limit toward η Tau, $n \leq 3.5$ cm^{-3}, an order of magnitude below our determination.

4.3.2. *Ultraviolet-Pumping Model of* H_2 *Rotational Excitation*

An alternative approach to obtaining the physical conditions of the diffuse clouds near the Pleiades involves the distribution of H_2 column densities in the $J = 0$, 1, and 4 rotational levels of the ground vibrational state. Much of this analysis, adapted from Lee et al. (2002), is derived from the work of Jura (1974, 1975), who showed that the $J = 4$ and 5 rotational levels of H_2 are populated primarily by photon pumping. In environments of low-to-moderate density, these levels will be depopulated by spontaneous emission. Thus, the relative populations of higher and lower rotational levels should indicate the density of the gas. While there may be other sources of excitation active in these clouds, such as collisions in shocked gas, the present model considers an extreme case in which all rotational excitation is due to UV pumping. Here, again, we assume steady state conditions and obtain an expression for the gas density from equation (3) of Lee et al. (2002) adopting a H_2 formation rate coefficient, $R = 3 \times 10^{-17}$ cm^3 s^{-1}, appropriate for Galactic clouds. The expression is

$$n = 9.2 \times 10^7 \frac{N(4)}{N_{tot}(H)} \left\{ \frac{0.26N(0)}{0.11[N(0) + N(1)]} + 0.19 \right\}^{-1}, \quad (4)$$

where $N(J)$ is the H_2 column density in rotational level J and the total hydrogen column density is found from $N_{tot}(H) = 2N(H_2)/f(H_2) = 2[N(0) + N(1)]/f(H_2)$. In this case, therefore, n is directly proportional to f. Column (9) of Table 6 presents the density estimates derived from equation (4) for the three sight lines with H_2 column densities measured by *Copernicus* (Spitzer et al. 1974; Savage et al. 1977; Frisch & Jura 1980). Unfortunately, only one of the sight lines, that toward η Tau, has a corresponding value from the $N(CH)/N(CH^+)$ method. Nevertheless, the densities obtained from equation (4), $n = 89$, 48, and 83 cm^{-3} for 20 Tau, 23 Tau, and η Tau, respectively, are consistently larger than those from the previous method by about a factor of 2. Here we exploit the opposite dependence of n on f exhibited in equations (2) and (4) to constrain both the density and the molecular fraction. Table 7 shows the effect on n calculated from the two methods as f is decreased slightly from 0.1 to 0.05. The analysis finds that a value of $f = 0.07$ provides the best agreement among the various density estimates, a value consistent with the average value of f for sight lines in Scorpius (Savage et al. 1977). The density toward η Tau for this value of f is then $n = 62$ cm^{-3}.

Lee et al. (2002) derived another expression that relates the gas density to the ambient UV radiation field. We can use this relation to determine I_{UV} based on the H_2 column densities in Table 6. From equation (4) of Lee et al. (2002) and using the above value for R,

$$I_{UV} = \frac{7.1 \times 10^{-23} n}{0.11 \beta_0} \left[\frac{N_{tot}(H)}{2f(H_2)} \right]^{1/2}, \quad (5)$$

where $\beta_0 = 5 \times 10^{-10}$ s^{-1} is the H_2 photoabsorption rate corresponding to the average Galactic field and the factor 0.11 represents the fraction of absorptions leading to H_2 dissociation. The

TABLE 7
DENSITY AS A FUNCTION OF $f(H_2)$

	n (cm^{-3}) FROM CH/CH^+			n (cm^{-3}) FROM H_2		
STAR	$f = 0.10$	$f = 0.07$	$f = 0.05$	$f = 0.10$	$f = 0.07$	$f = 0.05$
20 Tau	≤ 16	≤ 23	≤ 32	89 ± 34	62 ± 24	44 ± 17
	≤ 16	≤ 22	≤ 31	...	...	...
23 Tau	≤ 192	≤ 274	≤ 384	48 ± 12	34 ± 8	24 ± 6
	≤ 14	≤ 19	≤ 27	...	...	...
η Tau	46 ± 9	66 ± 14	92 ± 19	83 ± 20	58 ± 14	41 ± 10
27 Tau	16 ± 6	22 ± 9	31 ± 13	...	...	...
28 Tau	40 ± 6	56 ± 8	79 ± 12	...	...	...

I_{UV} values calculated from equation (5) are given in column (10) of Table 6. While there are only three determinations, each is smaller by approximately a factor of 2 compared to the values in column (4) calculated from the parameters in White (1984b). However, since equation (5) has no explicit x-dependence, we can determine what value of x brings our I_{UV} values into agreement. Solving equation (3) for x and using I_{UV} from column (10) of Table 6 yields $x = 0.9$, 1.1, and 1.3 pc for 20 Tau, 23 Tau, and η Tau, respectively. These are to be compared to the distances obtained from White (1984b) for the same three stars, $x = 0.30$, 0.32, and 0.72 pc, the values initially used in equation (3) to calculate the I_{UV} values in column (4) of Table 6. By substituting equation (4) for n into equation (5), it can be shown that this formula for I_{UV} is also independent of $f(H_2)$. Thus, if the larger distances just calculated were used in the comparative density analysis above, our best-match value of f would decrease slightly to 0.06, thereby decreasing the density toward η Tau to 52 cm^{-3}.

Despite the generally good agreement found from the above chemical models, the solutions are not unique, and the number of free parameters certainly does not eliminate the need for further refinement. One example would be the application of a time-dependent model of CH^+ formation in this environment. Assuming a flow rate for the gas with respect to the cluster of 10 km s^{-1} (Gordon & Arny 1984) and a cloud thickness of 0.1 pc (White 1984a), the timescale for cloud-cluster interactions is $\sim 10^4$ yr. A corresponding timescale for H_2 dissociation can be approximated by $1/G(H_2)$, where $G(H_2) \simeq 0.11\beta_0$ is the H_2 photodissociation rate given above. If self-shielding is also included, the dissociation rate would be lower by at least a factor of 10, yielding a characteristic timescale of $\sim 6 \times 10^3$ yr. Because the respective timescales are comparable, we cannot decouple the two processes, and time-dependent effects must ultimately be incorporated into any chemical model adopted to derive physical conditions.

4.3.3. *Diffuse-Cloud Model for* CH *and* CN

Following the analysis of CH and CN chemistry by Pan et al. (2005), we obtained a value for the gas density of the Pleiades molecular cloud toward HD 23512. The model is appropriate for a diffuse cloud with large molecular content but does not include dark cloud chemistry. As argued by Federman & Willson (1984), the CO column density from the densest, most opaque portion of the cloud, $N(CO) \sim 4.5 \times 10^{17}$ cm^{-2}, while larger than the values measured in diffuse gas, is significantly lower than those measured toward the centers of dark clouds. The Pleiades cloud is not, therefore, an intermediate zone between diffuse and dark clouds but simply a much less opaque molecular cloud than is normally observed in the Taurus region. Using our measured CH and CN column densities toward HD 23512 and setting $I_{UV} = 1$ due to the position of this star almost a parsec distant (in projected separation) from the luminous cluster stars, the model suggests $n > 1600$ cm^{-3}. The original study by Federman & Willson (1984) predicted $n \sim 300$–500 cm^{-3} based on their ^{13}CO data and the large velocity gradient model of Goldsmith et al. (1983). J. Bally & R. E. White (1986, unpublished; see White 2003) found a density of 300 cm^{-3} within 10′ of the position of peak CO emission and 800 cm^{-3} at the position of the peak. The consistency of these densities with those derived by Federman & Willson (1984) leads us to conclude that our lower limit is in error, being a factor of 2 larger than even the above peak value. Evidently, there is more CN along this line of sight than can be attributed solely to diffuse cloud chemistry. The chemical reaction network common to dark clouds appears to contribute to CN production despite the unusually low density of this diffuse molecular cloud.

5. DISCUSSION

In § 4.1 the relatively straightforward distribution of molecular gas in the Pleiades as traced by the molecules of CH^+, CH, and CN is contrasted with the rather complicated structures seen in the ionized atomic gas traced by Ca II. The largest columns of molecular gas are associated with a velocity component at $v_{LSR} \sim +9.5$ km s^{-1} concentrated in the western region of the cluster. Clearly, some of this material is related to the molecular cloud seen along the line of sight toward HD 23512, particularly that detected in CH and CN absorption in this direction. Indeed, the velocities of the CH and CN components here are consistent with the cloud velocity determined from molecular line emission by Federman & Willson (1984), and although the density of the cloud derived from our CH and CN column densities ($n > 1600$ cm^{-3}) is significantly larger than their predicted value ($\sim$300–500 cm^{-3}), the inclusion of dark cloud chemistry should correct this discrepancy. Still, whether or not all molecular components that share the cloud velocity have a common origin remains elusive. The general conclusions of the expansive study by White (2003) favor a three-body encounter in which gas associated with the Taurus dust clouds and redshifted by the interaction with the Pleiades accounts for some of the red components and a separate cloud approaching from the west and also interacting with the cluster accounts for others. In support of the latter, the strongest components of CH^+ absorption are located northwest of the cluster center, with a position and orientation similar to that of the western cloud described by White (2003). The absence of any corresponding CH components in this region indicates the low density of the material. Gas toward 17 Tau and 23 Tau with a velocity of +10 km s^{-1} likely probes the low-density envelope of the molecular cloud that lies just to the south of these sight lines. The rest of the

CH^+ components near +9 km s^{-1} may also trace this envelope, but the data do not preclude a connection with redshifted Taurus material.

The other, weaker constituent of molecular gas in the Pleiades has a velocity of $\sim$+7 km s^{-1}, associating it with the central component of atomic gas and with the Taurus clouds. All sight lines with detectable amounts of CH, except that toward HD 23512, and the majority of CH^+ sight lines exhibit this component. It is found in both species along sight lines to three stars in the center of the cluster (η Tau, 27 Tau, and 28 Tau), and these show similar CH/CH^+ column density ratios (0.2 for η Tau and 0.1 for 27 Tau and 28 Tau). Toward HD 23512, where both species are detected at $\sim$+9.5 km s^{-1}, the ratio is much larger (0.9). That the column densities of CH and CH^+ are well correlated for the central component strengthens the claim that CH toward most of the Pleiades is CH^+-like. The larger ratio toward HD 23512 results from the addition of CN-like CH to the total CH column and reinforces the idea that this sight line effectively probes the molecular cloud.

The patterns exhibited in the velocity components of Ca II (Fig. 8) offer unique insight into the complex interactions between the ISM and the stars of the Pleiades. For instance, the central component at $v_{LSR} \sim +7$ km s^{-1} seen toward all of the stars in our survey does not have a uniform velocity across the cluster. The slight blueshifts and redshifts apparent in Figures 8*d* and 8*f*, respectively, are a strong indication that a dynamical interaction is occurring in which cloud material passing through the UV radiation field of the cluster is deflected toward and away from our line of sight. That the pattern seems to repeat itself at larger and smaller velocities (Figs. 8*c* and 8*g*) suggests that the encounter of this central component can account for at least some of the observed red and blue components. Gas detected at velocities higher than $\sim$+10 km s^{-1} likely derives from multiple sources. The feature seen in Figure 8*h* may contain components missing from the gas in Figure 8*g* that have been further redshifted by cluster interactions, but may also contain independent components from a chance meeting with a second approaching cloud. The latter is the probable source of the extreme-velocity components in Figure 8*i* due to the proximity of these sight lines to the molecular cloud. The shocked atomic components in Figures 8*a* and 8*b* show additional indications of a velocity gradient from the center of the cluster to the northwestern edge, despite the noticeable gap toward 17 Tau, 20 Tau, and 22 Tau. In general, the various components of Ca II are more pervasive in number and extent than those in the analysis of Na I observations by White (2003), as expected if Ca II is the most widely distributed species as in Figure 6 of Pan et al. (2005). Clearly, highly sensitive observations of Ca II can trace the intricate cloud-cluster and cloud-cloud interactions of the Pleiades in greater detail and on a larger scale than Na I observations of equal quality.

An important result of our analysis of Na I/Ca II ratios (§ 4.2) was that they predicted the proper relationship between velocity components and the expected physical conditions of the associated clouds, strengthening our confidence in the column densities derived from our observations. Na I/Ca II ratios of order a few to 10 were measured for most positive-velocity components, indicating the diffuse nature of much of the interstellar gas near the cluster where calcium is not efficiently depleted onto the surfaces of dust grains. A ratio of order 100 was observed in the +9.2 km s^{-1} component toward HD 23512, since this gas lies in a denser region near the molecular cloud, an environment that results in higher calcium depletion. Final confirmation comes from the +6.2 km s^{-1} component toward this star whose Na I/Ca II ratio of $\sim$10 rightly places it among the diffuse components.

The precise density estimates of § 4.3 can place meaningful constraints on the chemical processes active in the diffuse clouds of the Pleiades. A comparison of the values obtained from CH/CH^+ column density ratios with those from rotationally excited H_2 column densities offers particular insight. We find generally good agreement in the densities obtained from the two methods by adopting a molecular fraction of $f = 0.07$. This value of f yields typical densities of $\sim$50 cm^{-3}, significantly below earlier predictions that favored densities between 100 cm^{-3} (Gordon & Arny 1984) and 400 cm^{-3} (White 1984a, 1984b). A possible discrepancy with our more precise estimates comes from the recent study by Zsargó & Federman (2003), who inferred a density upper limit of $n \leq 3.5$ cm^{-3} from the column densities of the fine-structure levels of C I toward η Tau. This determination is an order of magnitude lower than our value toward η Tau, $n = 62$ cm^{-3}, obtained from both CH/CH^+ ratios and H_2 rotational populations. Yet, based on their density estimate, Zsargó & Federman (2003) predicted a CH column density upper limit toward η Tau of $N(CH) \leq 7.3 \times 10^{11}$ cm^{-2}, consistent with our measured value of 4.8×10^{11} cm^{-2}. To derive this predicted column density, the authors incorporated nonthermal motions of ions and neutrals due to the propagation of Alfvén waves in a transition zone between cloud and intercloud material (Federman et al. 1996b). Without incorporating turbulence, the predicted column density along this sight line is $N(CH) \leq 1.6 \times 10^9$ cm^{-2}, much lower than the measured value. Nonthermal models hold great promise for diffuse cloud chemistry, particularly in explaining the abundance of the CH^+ radical as well as the abundances of molecules such as CH, which are tied to its formation.

The question remains, then, why the density predicted by Zsargó & Federman (2003) is so much lower than our value. Two possibilities immediately present themselves. First, observations of H_2, CH, and CH^+ may sample different cloud depths due to the stratification of molecular species along the line of sight. This scheme suggests that rotationally excited H_2 molecules probe denser portions of the cloud closer to the stars, in the main portion of the photodissociation region (PDR), where the UV radiation is strongest and is responsible for populating the higher J-levels through UV pumping. CH and CH^+, as well as C I, would then trace the less dense outer portions of the cloud away from the PDR. A major drawback to this scenario is it requires $f = 0.5$ or higher to yield low enough densities from our measured CH/CH^+ column density ratios to agree with the C I result, which would subsequently increase our H_2-derived densities for this diffuse gas to greater than 400 cm^{-3}, a value more typical of the Pleiades molecular cloud. A more suitable alternative is that the fine-structure levels of C I trace regions of various extent along the line of sight. If the $J = 1$ level, for instance, was confined to a region of space 1/10 the size of that occupied by the $J = 0$ level, the density upper limit would be more in line with our determination. Finally, the inclusion of time-dependent effects into a chemical model of CH^+ formation may still prove to be important, since the timescale for H_2 dissociation is comparable to the characteristic time in which the cloud is interacting with the cluster. Because the initiating reaction leading to CH production requires H_2, a decreasing presence due to photodissociation would demand a higher density to account for the observed columns of CH. Such a requirement could be accommodated by our simple steady state model by, again, raising slightly the value of $f(H_2)$.

The most general conclusion of this investigation is that detailed observations of both atomic and molecular species essentially confirm the scenario of cloud-cluster interactions constructed by White (2003). A pervasive foreground gas cloud at

$v_{LSR} \sim +7$ km s^{-1} seen toward nearly every star in both strong atomic and weaker molecular absorption is flowing through the cluster and dynamically interacting with the stellar UV radiation field. The clearly symmetric patterns of both blueshifted and redshifted Ca II components extending across the cluster demonstrate the large-scale nature of these interactions. A second cloud at $v_{LSR} \sim +10$ km s^{-1} is also likely to be interacting with the cluster due to the strong CH^+ absorption near this velocity northwest of the cluster center and the existence of a diffuse molecular cloud also at $v_{LSR} \sim +10$ km s^{-1} to the southwest. High-velocity Ca II components with no direct connection to redshifted foreground gas may also require the existence of a second interacting cloud.

6. SUMMARY

Twenty stars in the Pleiades were observed with high resolution and high signal-to-noise ratio in a spectral range allowing for the detection of absorption features from CN, Ca II K, Ca I, CH^+, and CH. Total equivalent widths are consistent with previous determinations except in cases where we detect weaker features owing to our greater sensitivity. Mean *b*-values for CN, CH^+, and CH indicate that toward most of the Pleiades CH is linked to the formation of CH^+ rather than to CN chemistry. Weighted mean velocities for individual species reveal a kinematic separation of atomic and molecular gas, with neutrals more closely associated with the latter. For the molecular species, two distinct velocity components are sufficient to characterize the observed profiles, with the sight line toward HD 23512 clearly probing the molecular cloud seen in this direction. Considerably more structure is seen along lines of sight in the atomic gas traced by Ca II. Velocity gradients are apparent in the pervasive central component implying a dynamical interaction with the cluster. Density estimates from CH/CH^+ column density ratios agree well with those based on the rotational excitation of H_2 molecules for $f(H_2) = 0.07$, yielding typical densities of $\sim$50 cm^{-3} for the ISM near the Pleiades. However, given the similar timescales of the relevant chemical and dynamical processes, the importance of time-dependent effects must be examined.

With the availability of high-quality absorption-line data for CN, Ca II, Ca I, CH^+, and CH provided by this investigation and for Na I provided by White et al. (2001), existing models of interstellar chemistry must now be improved and brought to bear on the complex interaction between diffuse gas and the Pleiades cluster. The precise densities determined here must be incorporated into any model describing the interaction, and all phenomenon must be treated self-consistently. The application of a time-dependent model, in particular, will likely prove necessary.

We thank Yaron Sheffer for his help in synthesizing CH profiles and Dan Welty for his very useful comments on an earlier draft of this paper. We also acknowledge the thorough examination of our calculations by the anonymous referee that led to more consistent results. This research made use of the Simbad database operated at CDS, France. M. Martinez participated in the Research Experience for Undergraduates at the University of Toledo under NSF-REU grants PHY-0097367 and 0353899. The research presented here was also supported in part by NASA Long Term Space Astrophysics grant NAG5-4957 to the University of Toledo.

REFERENCES

Crane, P., Lambert, D. L., & Sheffer, Y. 1995, ApJS, 99, 107
Crawford, I. A. 1992, MNRAS, 259, 47
Crawford, I. A., Barlow, M. J., & Blades, J. C. 1989, ApJ, 336, 212
Draine, B. T., & Katz, N. 1986, ApJ, 306, 655
Elitzur, M., & Watson, W. D. 1978, ApJ, 222, L141
———. 1980, ApJ, 236, 172
Falgarone, E., Verstraete, L., Pineau des Forêts, G., & Hily-Blant, P. 2005, A&A, 433, 997
Federman, S. R. 1982, ApJ, 257, 125
Federman, S. R., & Huntress, W. T. 1989, ApJ, 338, 140
Federman, S. R., Rawlings, J. M. C., Taylor, S. D., & Williams, D. A. 1996a, MNRAS, 279, L41
Federman, S. R., Strom, C. J., Lambert, D. L., Cardelli, J. A., Smith, V. V., & Joseph, C. L. 1994, ApJ, 424, 772
Federman, S. R., Weber, J., & Lambert, D. L. 1996b, ApJ, 463, 181
Federman, S. R., & Willson, R. F. 1984, ApJ, 283, 626
Frisch, P. C. 1972, ApJ, 172, 301
Frisch, P. C., & Jura, M. 1980, ApJ, 242, 560
Gredel, R., van Dishoeck, E. F., & Black, J. H. 1993, A&A, 269, 477
Goldsmith, P. F., Young, J. S., & Langer, W. D. 1983, ApJS, 51, 203
Gordon, K. J., & Arny, T. T. 1984, AJ, 89, 672
Hawkins, I., & Jura, M. 1987, ApJ, 317, 926
Herbst, E. 1978, ApJ, 222, 508
Hobbs, L. M. 1973, ApJ, 181, 79
———. 1976, ApJ, 206, L117
Joulain, K., Falgarone, E., Pineau des Forêts, G., & Flower, D. 1998, A&A, 340, 241
Jura, M. 1974, ApJ, 191, 375
———. 1975, ApJ, 197, 581
———. 1977, ApJ, 218, 749
Lambert, D. L., Sheffer, Y., & Crane, P. 1990, ApJ, 359, L19
Lee, D.-H., et al. 2002, ApJ, 575, 234
Marschall, L. A., & Hobbs, L. M. 1972, ApJ, 173, 43
Morton, D. C. 1991, ApJS, 77, 119
Pan, K., Federman, S. R., Cunha, K., Smith, V. V., & Welty, D. E. 2004, ApJS, 151, 313
Pan, K., Federman, S. R., Sheffer, Y., & Andersson, B.-G. 2005, ApJ, 633, 986
Perryman, M. A. C., ed. 1997, The *Hipparcos* and Tycho Catalogues (ESA SP-1200; Noordwijk: ESA)
Pineau des Forêts, G., Flower, D. R., Hartquist, T. W., & Dalgarno, A. 1986, MNRAS, 220, 801
Routly, P. M., & Spitzer, L., Jr. 1952, ApJ, 115, 227
Savage, B. D., Bohlin, R. C., Drake, J. F., & Budich, W. 1977, ApJ, 216, 291
Siluk, R. S., & Silk, J. 1974, ApJ, 192, 51
Spitzer, L., Jr., Cochran, W. D., & Hirshfeld, A. 1974, ApJS, 28, 373
Tull, R. G., Macqueen, P. J., Sneden, C., & Lambert, D. L. 1995, PASP, 107, 251
Vallerga, J. V., Vedder, P. W., Craig, N., & Welsh, B. Y. 1993, ApJ, 411, 729
Vanden Bout, P. A., & Snell, R. L. 1980, ApJ, 236, 460
Vanden Bout, P. A., & Thaddeus, P. 1971, ApJ, 170, 297
Vejby-Christensen, L., Andersen, L. H., Heber, O., Kella, D., Pedersen, H. B., Schmidt, H. T., & Zajfman, D. 1997, ApJ, 483, 531
Welty, D. E., Federman, S. R., Gredel, R., Thorburn, J. A., & Lambert, D. L. 2006, ApJS, 165, 138
Welty, D. E., Hobbs, L. M., & Morton, D. C. 2003, ApJS, 147, 61
Welty, D. E., Morton, D. C., & Hobbs, L. M. 1996, ApJS, 106, 533
White, R. E. 1973, ApJ, 183, 81
———. 1984a, ApJ, 284, 685
———. 1984b, ApJ, 284, 695
———. 2003, ApJS, 148, 487
White, R. E., Allen, C. L., Forrester, W. B., Gonnella, A. M., & Young, K. L. 2001, ApJS, 132, 253
White, R. E., & Bally, J. 1993, ApJ, 409, 234
Younan, K. F., & Dufton, P. L. 1984, MNRAS, 209, 123
Zsargó, J., & Federman, S. R. 2003, ApJ, 589, 319